

## COMPUTATIONAL METHODS FOR NON-NEWTONIAN POWER LAW FLUIDS

<sup>1</sup>Dr.P.Kavitha

<sup>1</sup>Dr.P.kavitha is currently working as Lecture in mathematics from Telangana social welfare residential degree college forwomen,Karimnagar,Telangana

Received: 06.04.2020

Revised: 08.05.2020

Accepted: 03.06.2020

### Abstract

In this book we present a simplified method for non-Newtonian power-law fluid flows expansions. The new strategy embraces the indicator corrector conspires and recreates answers for the naturally visible conditions recovered from the cross-section Boltzmann condition through Chapman-Enskog extension investigation. The shortened force law model is fused into this strategy to locally modify the physical consistency and the related unwinding parameter, which recuperates the non - Newtonian practices. Contrasted and existing non-Newtonian cross-section Boltzmann models, the proposed technique legitimately advances the naturally visible factors rather than the circulation capacities, which disposes of the inborn disadvantages like significant expense in virtual memory and awkward execution of physical limit conditions. The legitimacy of the strategy is shown by benchmark tests and correlations with an investigative arrangement or numerical outcomes in the writing. Benchmark answers for the three-dimensional cover driven hole stream of non-Newtonian force law liquid are additionally accommodated future reference".

**Keywords:** non-Newtonian power-law fluid flows, physical limit, parameter

© 2020 by Advance Scientific Research. This is an open-access article under the CC BY license (<http://creativecommons.org/licenses/by/4.0/>)  
DOI: <http://dx.doi.org/10.31838/jcr.07.13.04>

### INTRODUCTION

Non-Newtonian fluid refers to a specific category of fluid which exhibits variable viscosity under the action of force. It certainly differs from the Newtonian fluid which follows Newton's law of viscosity and bears constant viscosity under stress. The physical viscosity in non-Newtonian fluids could be dependent on the magnitude of the shear stress (e.g., shear-thickening/dilatant fluids, shear-thinning/pseudoplastic fluids, Bingham plastics, etc.) or even time-dependent (e.g., thixotropic liquids, rheopectic liquids, etc.). In fact, many practical fluids may present these non-Newtonian behaviors. Typical examples include blood, silicone oils, printer ink, polymers, etc.

Numerical interpretation of the non-Newtonian behaviors thus becomes an important topic from both the academic and the application points of view. Explorations in this topic have been continuing for over a century; and many mathematical models have been constructed, which include the generalized Newtonian models, the linear or elementary nonlinear viscoelastic models, the models with memory-integral expansion, etc. Specifically, the generalized Newtonian fluid models maintain the general form of governing equations for Newtonian fluid while making the viscosity dependent on the shear rate [1]. The linear viscoelastic models, which were initially proposed

equations that govern the fluid system. One popular mathematical interpretation is the lattice Boltzmann equation (LBE) or the lattice Boltzmann method (LBM) which is a mesoscopic method developed on the kinetic theory. In LBM, the distribution function is the primitive variable that is directly evolved; and the conservative variables and fluxes at the macroscopic scale can be obtained by moments of the distribution functions in the velocity space. The LBM seems to be more attractive than conventional Navier-Stokes (N-S) solvers in some aspects like the kinetic nature, simplicity and explicitness. Being constructed at the mesoscopic scale, LBM is a more general model than the N-S equations in describing fluid behaviors. Its evolution of distribution functions is essentially accomplished in the velocity space rather than in the physical space; and the whole process is in a linear and explicit manner. The discretization of the nonlinear convection terms in the N-S

by Maxwell [2], essentially establish a linear differential relationship between the stress tensor and the shear rate. Later, the elementary nonlinear viscoelastic model tracks the evolution of a particular fluid particle and thus consolidates the nonlinear convection effect into the constitutive relation, which makes the model more "objective" [3, 4]. More recently, some models were proposed by the memory-integral expansion strategy [5, 6], which assumes that the stress in a fluid element is only dependent on its own kinetic history and can thus be achieved by integrations over time. Among these approaches of constructing non-Newtonian models, the generalized Newtonian fluid models seem to be the simplest and the most straightforward way due to the similarity to the Newtonian expressions. And the most commonly used one in this category might be the power-law model [7]. In this model, the local viscosity is assumed to follow an exponential relationship with the shear rate. By adjusting the power index, typical non-Newtonian behaviors like the shear-thinning or the shear-thickening can be interpreted. In this work, the power-law model will be adopted to study non-Newtonian fluid flow".

### Non-Newtonian Fluid Models

Thenon-Newtonianmodelsareessentialconstitutiverelationsandshouldbeconsolidatedintospecific

equations are thus avoided, and the scheme can be conveniently parallelized.

Efforts have been made in incorporating the non-Newtonian models into the LBM to recover and investigate this distinct physical phenomenon. The earliest attempt might be 4 This article is protected by copyright. All rights reserved. carried out by Aharonov and Rothman [8] who used the conventional single-relaxation-time (SRT) lattice Boltzmann model as the flow solver. Gabbanelli et al. [9] recognized that the SRT model might be unstable at extreme values of the relaxation parameter and thus implemented a truncated power-law model which sets upper and lower limits to the fluid viscosity. Giraud et al. [10] and Sullivan et al. [11] both explored the simulations in threedimensional scenarios. Yoshino et al. [12] proposed an alternative model which decouples the relaxation parameter from the viscosity by

consolidating the shear stress into the equilibrium distribution functions. And this model was then modified by Wang et al. [13] to ensure mass conservation. Apart from the SRT model, a few lattice Boltzmann models with multiple relaxation-time (MRT) were also proposed for simulations of non-Newtonian fluid flows [14, 15]. Other than developing non-Newtonian lattice Boltzmann schemes, abundant examples of applying lattice Boltzmann models in investigations of non-Newtonian phenomena can also be found in literature [16-22].

Although being an important candidate in resolving non-Newtonian problems, the lattice Boltzmann models may not be the mainstream solution to this category of problems. Limitations of LBM, e.g., high cost in virtual memory, inconvenient implementation of physical boundary conditions, and poor numerical stability in small viscosity scenario, are somehow intrinsic and hard to be removed [23-25]. The first two limitations originate from the cornerstone of LBM, which is the evolution of distribution functions. The number of distribution functions at each mesh point is much larger than the number of macroscopic variables. Therefore, more virtual memory would be consumed. In the meantime, the physical boundary conditions which are related to the macroscopic variables should be converted to boundary conditions for the distribution functions as to be implemented in the conventional lattice Boltzmann framework. Such transformation is tedious and sometimes difficult for certain boundary conditions or complex geometries. In addition, the stability analysis suggested that the lattice Boltzmann method with single relaxation parameter would become unstable when the relaxation parameter approaches 0.5 [23], which is equivalent to the condition of small physical viscosity. Some strategies have been proposed to alleviate the stability issue, which include the multiple-relaxation-time model [26], the entropic LBGK method [27], the regularized lattice

Boltzmann equation [28] etc. However, all these attempts are carried out within the conventional framework and thus cannot remove the first two limitations of LBM.

The simplified lattice Boltzmann method (SLBM) is a recent exploration towards eliminating or alleviating limitations of the conventional LBM [29, 30]. Instead of directly evolving the distribution functions, SLBM reconstructs solutions to the macroscopic equations recovered from LBE through the Chapman-Enskog expansion analysis. The second order accuracy is preserved in the reconstruction process and the final formulations reflect direct evolution of the macroscopic variables. Consequently, the dependent variables of distribution functions in the conventional LBM are replaced by the macroscopic flow variables in the SLBM, which reduces the number of variables at each mesh point (see Table 1); the physical boundary conditions can be implemented straightforwardly; and the flexibility of the method on non-uniform or body-fitted meshes is enriched. Moreover, the von Neumann stability analysis indicates that SLBM is stable at all wavenumbers in high Reynolds number scenario [29], which makes it a competitive candidate for real engineering problems. The idea of SLBM has been applied in various fluid problems such as the thermal flows, fluid-structure interaction, axisymmetric flows, multiphase flows etc. [31-34]. Yet its extension to the non-Newtonian simulations has not been reported. Although the idea is similar to its Newtonian counterpart, detailed derivations and the final formulations of the method for non-Newtonian flows would differ since the physical viscosity would be coupled with the flow field. In this paper, we will present the simplified lattice Boltzmann method for non-Newtonian power-law fluids and give comprehensive evaluation of its performance in simulations.

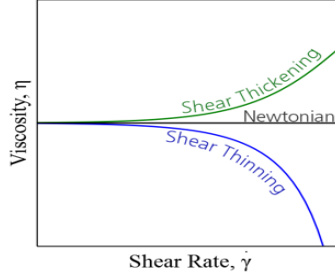


Figure: 1.1. Newtonian rate

The remaining parts of this paper are organized as follows. Section 2 briefs the lattice Boltzmann method and the power-law model for non-Newtonian fluids. Further explanation on the truncated power-law model and detailed derivation of its association with the simplified lattice Boltzmann method are presented in Section 1.3. Numerical validations of the proposed method are carried out in Section 1.4, based on which benchmark solutions to some problems are given. Finally, Section 1.5 remarks the conclusions of this work .

### Lattice Boltzmann Method and The Power-Law Model

#### Lattice Boltzmann Method

The lattice Boltzmann method (LBM) resolves the flow field by updating the distribution function  $f_\alpha$ , which follows the lattice Boltzmann equation (LBE) as shown below:

$$f_\alpha(r + e_\alpha \delta_t, t + \delta_t) = f_\alpha(r, t) + \frac{f_\alpha^{eq}(r, t) - f_\alpha(r, t)}{\tau} \quad (1.1)$$

Where  $r$  and  $t$  are the location vector and the time level, respectively;  $\tau$  is the single relaxation parameter in the BGK

collision model;  $e_\alpha$  is the lattice velocity vector along the  $\alpha$ -th direction;  $\delta t$  represents the time interval; the superscript  $eq$  denotes the equilibrium state of the distribution function

$$f_\alpha^{eq} = P W_\alpha \left[ 1 + \frac{e_\alpha \cdot u}{c_s^2} + \frac{(e_\alpha \cdot u)^2 - (c_s |U|)^2}{2c_s^4} \right] \quad (1.2)$$

Here,  $\rho$  and  $u$  respectively denote the density and the velocity vector;  $\omega_\alpha$  and  $c_s$  are the weighting coefficient and the sound speed, respectively. For typical D2Q9 model, we have

$$e_\alpha = \begin{cases} 0 \\ (\pm 1, 0), (0, \pm 1) \\ (\pm 1, \pm 1) \end{cases} \quad (1.3)$$

$$\omega_0 = \frac{4}{9} \omega_{1-4} = \frac{1}{9} \omega_{5-8} = \frac{1}{36} C_s = \frac{c}{\sqrt{3}} \quad (1.4)$$

$$\begin{aligned} \alpha &= 0 \\ \alpha &= 1, 2, 3, 4 \\ \alpha &= 5, 6, 7, 8 \end{aligned}$$

And the D3Q15 model gives

$$e_\alpha = \begin{cases} 0 \\ (\pm 1, 0, 0), (0, \pm 1, 0), (0, 0, \pm 1) \\ (\pm 1, \pm 1, \pm 1) \end{cases} \quad (1.5)$$

$$\omega_0 = \frac{2}{9}\omega_{1-6} = \frac{1}{9}\omega_{7-14} = \frac{1}{72}C_s = \frac{c}{\sqrt{3}} \quad (1.6)$$

Where  $c = \delta x / \delta t$  is the lattice velocity, and  $\delta x$  is the lattice spacing.

### Chapman-Enskog expansion analysis

The lattice Boltzmann equation (LBE) is believed to be an interpretation of more general fluid behaviors spanning from the continuum regime to the slip flow regime. Specifically, in the continuum flow regime, LBE is consistent to the macroscopic Navier-Stokes equations with desired order of accuracy. Such consistency can be constructed through the Chapman-Enskog (C-E) expansion analysis.

The C-E analysis of the LBE starts from the multi-scale expansions of the distribution function, temporal and spatial derivatives in terms of a parameter  $\varepsilon$  that is proportional to the Knudsen number, which gives

$$f_\alpha = f_\alpha^{(0)} + \varepsilon f_\alpha^{(1)} + \varepsilon^2 f_\alpha^{(2)} \quad (1.7)$$

$$\frac{\partial}{\partial t} = \varepsilon \frac{\partial}{\partial t_0} + \varepsilon^2 \frac{\partial}{\partial t_1} \quad (1.8)$$

$$\Delta_r = \varepsilon \nabla_r \quad (1.9)$$

Performing Taylor-series expansion on Eq. (1) yields

$$\left[ \frac{\partial}{\partial t} + e_\alpha \cdot \nabla \right] f_\alpha + \frac{\delta_t}{2} \left[ \frac{\partial}{\partial t} + e_\alpha \cdot \nabla \right]^2 f_\alpha + \frac{1}{\tau \delta_t} (f_\alpha - f_\alpha^{eq}) + o(\delta_t^2) = 0 \quad (1.10)$$

Substituting Eqs. (7)-(9) into the above equation and consolidating obtained formulations at different scales, one can derive the following macroscopic equations

$$\frac{\partial p}{\partial t} + \nabla \cdot [\sum_\alpha e_\alpha f_\alpha^{eq}] = 0 \quad (1.11)$$

$$\frac{\partial p u}{\partial t} + \nabla \cdot \sum_\alpha (e_\alpha)_\beta (e_\alpha)_\gamma \left[ f_\alpha^{eq} + \left[ 1 - \frac{1}{2\tau} \right] f_\alpha^{neq} \right] = 0 \quad (1.12)$$

Where

$$f_\alpha^{neq} = -\tau \partial_t D f_\alpha^{eq} \quad (1.13)$$

Here,  $f_\alpha^{eq} = f_\alpha^{(0)}$ ,  $f_\alpha^{neq} = \varepsilon f_\alpha^{(1)}$ , and  $D = \left[ \frac{\partial}{\partial t} + e_\alpha \cdot \nabla \right]$ . and the relaxation parameter is related

to the kinematic viscosity  $\nu$  through

$$\nu = C_s^2 \delta_t (\tau - 0.5) \quad (1.14)$$

### The power-law model for non-Newtonian fluids

For non-Newtonian fluids, the physical viscosity is dependent on the local shear rate through the constitutive equation. A simply and widely used model for non-Newtonian fluid is the power-law model, which evaluates the local viscosity through

$$\mu = \mu_0 |\gamma|^{n-1} \quad (1.15)$$

where  $\mu = \rho \nu$  is the dynamic viscosity;  $\mu_0$  is the flow consistency coefficient; and  $n > 0$  denotes the power law index. Specifically, cases with  $n < 1$  respectively represent the shear-thinning (pseudoplastic) and the shear-thickening (dilatant) fluids, while the setting of  $n = 1$  recovers regular Newtonian fluid behaviours. The shear rate  $\gamma$  is defined as

$$\gamma = \nabla u + (\nabla u)^T \quad (1.16)$$

While its magnitude is calculated by

$$|\gamma| = \sqrt{\frac{2}{3} \sum_{\alpha, \beta} (e_\alpha)_\beta (e_\beta)_\alpha \left[ f_\alpha^{neq} + \left[ 1 - \frac{1}{2\tau} \right] f_\beta^{neq} \right]^2} \quad (1.17)$$

Correspondingly, the parameter should be locally adjusted for non-Newtonian fluid flows. And the local parameter is obtained by substituting Eq. (14) into

$$\alpha = 7 \sim 14$$

FOR

### Simplified Lattice Boltzmann Method for non-Newtonian Power-law Fluids Formulations

Following the idea of simplified lattice Boltzmann method (SLBM) for incompressible Newtonian fluid flows [29, 31], the derivation of the present model for non-Newtonian fluid flows starts from the macroscopic governing equations (11) and (12) recovered from LBE. Implementing the fractional step technique, the recovered equations can be resolved in the following predictor-corrector strategy:

**Predictor step:**

$$\frac{\partial p}{\partial t} + \nabla \cdot \sum_\alpha e_\alpha f_\alpha^{eq}(r, t) = 0 \quad (2.1)$$

$$\frac{\partial p u}{\partial t} + \nabla \cdot \sum_\alpha (e_\alpha)_\beta (e_\alpha)_\gamma \left[ f_\alpha^{eq} + \frac{1}{2\tau} f_\alpha^{neq} \right] = 0 \quad (2.2)$$

**Corrector step:**

$$\frac{\partial p}{\partial t} = 0 \quad (2.3)$$

$$\frac{\partial p u}{\partial t} + \nabla \cdot \sum_\alpha (e_\alpha)_\beta (e_\alpha)_\gamma \left[ 1 - \frac{1}{\tau} \right] f_\alpha^{neq} = 0 \quad (2.4)$$

The essential part of the derivation is to reconstruct solutions to these equations within the lattice Boltzmann framework. Specifically, in the predictor step, the intermediate flow variables are proposed to be

$$p^* = \sum_\alpha f_\alpha^{eq}(r - e_\alpha \delta_t, t - \delta_t) \quad (2.5)$$

$$p^* u^* = \sum_\alpha e_\alpha f_\alpha^{eq}(r - e_\alpha \delta_t, t - \delta_t) \quad (2.6)$$

Performing the Taylor-series expansion analysis on the above formulations and applying the relationships given by C-E analysis (Eq. (13)), it can be proven that, to the second order accuracy, Eqs. (22) and (23) recover solutions to the macroscopic equations (18) and (19) in the predictor step, respectively. Detailed proofs for this step can be found in the Appendix. In the corrector step, as shown in Eq. (20), no correction would be made on the intermediate density. To facilitate the derivation of the corrected velocity, Eq. (21) is rewritten into the following form with the help of Eq. (13):

$$\frac{\partial p u}{\partial t} - \nabla \cdot \sum_\alpha (e_\alpha)_\beta (e_\alpha)_\gamma \tilde{f}_\alpha = 0 \quad (2.7)$$

Where

$$\tilde{f}_\alpha = (\tau - 1) \delta_t D f_\alpha^{eq} \quad (2.8)$$

And its solution can be reconstructed by

$$p^{n=1} u^{n=1} = p^* u^* = \sum_\alpha e_\alpha \left[ \tilde{f}_\alpha(r + 0.5 e_\alpha \delta_t, t - 0.5 \delta_t) - \tilde{f}_\alpha(r - 0.5 e_\alpha \delta_t, t - 0.5 \delta_t) \right] \quad (2.9)$$

The consistency between Eq. (26) and Eq. (24) can be established through Taylor series expansion. It can be demonstrated that, to the second order accuracy in space and time, Eq. (26) is equivalent to Eq. (24). For reference, detailed derivations for this step are attached in the Appendix.

The remaining issue here is the approximation of the newly defined quantity  $f_{\alpha}^{\sim}$  at specific space and time levels. Since the recovery of Eq. (24) from Eq. (26) involves the space derivative of the second moment of  $f_{\alpha}^{\sim}$ , the approximated  $f_{\alpha}^{\sim}$  would be divided by the mesh spacing  $\delta x$  which is equal to  $\delta t$ . Thus, the approximation of  $f_{\alpha}^{\sim}$  should fulfill the third order accuracy of  $O(\delta t^3)$  in order not to deteriorate the overall second order accuracy. To fulfill that requirement, the approximated  $f_{\alpha}^{\sim}$  locates at the space/time level of  $(r \pm 0.5e_{\alpha}\delta t, t - 0.5\delta t)$ . In the meantime, given the fact that the marching in time levels is from  $(t-\delta t)$  to  $(t)$ , the shifting of half time step of  $f_{\alpha}^{\sim}$  in Eq. (26) facilitates establishing a central difference approximation which ensures the second order of temporal accuracy, and the following formulations can be derived

$$f_{\alpha}^{\sim}(r + 0.5e_{\alpha}\delta t, t - 0.5\delta t) = [\tau(r \pm 0.5\delta t - 0.5\delta t) - 1]\delta t Df_{\alpha}^{eq}(r \pm 0.5e_{\alpha}\delta t, t - 0.5\delta t) \quad (2.10)$$

$$\frac{\tau(r + 0.5e_{\alpha}\delta t, t - 0.5\delta t)}{\tau(r, t) + \tau(r \pm e_{\alpha}\delta t, t) + \tau(r, t - \delta t) + \tau(r \pm e_{\alpha}\delta t, t - \delta t)} = \quad (2.11)$$

$$\delta_t Df_{\alpha}^{eq}(r + 0.5e_{\alpha}\delta t, t - 0.5\delta t) = f_{\alpha}^{eq}(r + e_{\alpha}\delta t, t) - f_{\alpha}^{eq}(r, t - \delta t) + o(\delta t^3) \quad (2.12)$$

$$\delta_t Df_{\alpha}^{eq}(r - 0.5e_{\alpha}\delta t, t - 0.5\delta t) = f_{\alpha}^{eq}(r, t) - f_{\alpha}^{eq}(r - e_{\alpha}\delta t, t - \delta t) + o(\delta t^3) \quad (2.13)$$

Note that the intermediate properties obtained in the predictor step are utilized here as the physical properties at the time level of  $t$ .

Compared with conventional lattice Boltzmann models, the derived simplified lattice Boltzmann model (SLBM) could expect some intriguing merits while maintaining advantages of the conventional LBM such as the kinetic nature, simplicity and

explicitness. The final formulations of SLBM reflect evolution of macroscopic variables instead of the distribution functions. The equilibrium distribution function can be evaluated by the macroscopic properties, while the non-equilibrium distribution function is approximated by the difference of two equilibrium distribution functions that are also associated with the macroscopic variables. Thus, the minimum number of variables at each point for SLBM is the number of macroscopic flow properties (3 in two-dimensional cases). Even if storing the intermediate flow properties, the total number of variables at each mesh point is 6. In contrast, the dependent variables in the conventional LBM are the distribution functions. Therefore, the minimum number of variables at each mesh point is the number of lattice velocity directions (9 variables for D2Q9 model). Therefore, compared with the conventional LBM, 33.3% of virtual memory can be reduced by using the present SLBM with the D2Q9 model. In Table 1, the theoretical reduction rates of virtual memory for different lattice velocity models are provided. It should be noted that the expected reduction rates provided here are only for reference. The practical memory cost would be dependent on the programming skills and the compromise with computational efficiency.

In the meantime, by using the macroscopic flow variables as the dependent variables, the physical boundary conditions that are directly associated with the macroscopic flow variables can be implemented in a more straightforward way in the present SLBM. The tedious transformation into conditions for the distribution functions in the conventional LBM is thus removed. Moreover, the stability analysis of SLBM for Newtonian fluids reveals that it is more stable than conventional LB models [29], which is a favored characteristic for non-Newtonian simulations in which fluid viscosity exhibits large variations.

**Table 2.1 Comparison of numbers of variables at each mesh point**

Model	LBM	SLBM	Reduction rate
D2Q9	9	6	33.3%
D3Q15	15	8	46.7%
D3Q19	19	8	57.9%

### Truncated Power-Law Model

Direct implementation of the power-law model could lead to serious issues due to its unphysical limits at zero shear rates. Referring to Eqs. (15)-(17), at zero shear rates, the power-law model would give infinite viscosity for shear-thinning fluids while yielding zero viscosity for shear-thickening fluids. In the meantime, these two unphysical limits also pose numerical challenges for LBM. Within the lattice Boltzmann framework, fluid viscosity is reflected by the relaxation parameter  $\tau$ . The large viscosity and the inviscid condition correspond to large value of  $\tau$  and  $\tau=0.5$ , respectively. Previous studies indicated that the conventional LBM would become highly unstable when  $\tau$  approaching 0.5 [23], and show deteriorated numerical accuracy for  $\tau \geq 1$  [35]. To alleviate this issue, Gabbanelli et al. [9] proposed the truncated power-law model. By setting upper and lower limits for the fluid viscosity ( $\nu_{max}=0.1$  and  $\nu_{min}=0.001$  in their paper), the corresponding relaxation parameters vary within desired ranges ( $\tau_{max}=0.8$  and  $\tau_{min}=0.503$ ).

In the present study, we follow the similar way of adopting truncated power-law model, but directly implement limits for the relaxation parameter. As shown in the previous stability analysis for Newtonian fluid [29], SLBM bears very good numerical stability in the extreme case of  $\tau=0.5$ . Therefore, the lower limit is set as  $\tau_{min}=0.5$ . And the upper limit of the relaxation

parameter is  $\tau_{max}=1.2$  in all numerical examples, if not particularly specified. The larger adjustable range of the relaxation parameter could endow more flexibility when recovering non-Newtonian behaviors. Note that the local shear rate in Eq. (16) is calculated by the finite difference method.

### Implementation Of Boundary Conditions

As mentioned before, the evolution of macroscopic variables in SLBM allows direct implementation of physical boundary conditions without tedious transformation into boundary conditions for the distribution functions. For Dirichlet boundary conditions, boundary values of the physical properties can be directly assigned on the boundary mesh points. And normally, information on two inner layers of mesh points is utilized to evaluate boundary values when implementing Neumann boundary conditions, which ensures the second order accuracy in space.

It is noteworthy that the corrector step of SLBM requires the boundary values of the newly defined quantity  $f_{\alpha}^{\sim}$ . Recognizing that  $f_{\alpha}^{\sim}$  is continuous over the physical space, the linear extrapolation scheme is adopted here to determine its boundary value. This strategy has been adopted in the simulation of Newtonian fluid flows [30]. Given the fact that this quantity is a

minor term in the order of  $O(\delta t)$ , the linear extrapolation scheme would not deteriorate the global second order accuracy.

**Computational Sequence**

For illustration purposes, one possible procedure of implementing the proposed simplified lattice Boltzmann method for non-Newtonian power law fluid is presented as follows:

- (1) Mesh initialization. Specify the streaming distance  $\delta_x$  ( $\delta_x = \delta_x$ ).
- (2) Predictor step: use Eqs. (22) and (23) to evaluate intermediate flow properties  $\rho^*$  and  $u^*$ .
- (3) Calculate the non-equilibrium term  $f_{\alpha}^{\sim}$  using Eqs. (27)-(30).
- (4) Implement linear extrapolation scheme to determine boundary values of  $f_{\alpha}^{\sim}$ .
- (5) Corrector step: update the fluid velocity in the new time step with Eq. (26).
- (6) Implement appropriate physical boundary conditions for the macroscopic properties.
- (7) Repeat steps (2)-(6) until the computation is converged or the prescribed maximum iteration step is reached.

**Numerical Examples**

In this part, numerical tests on the plain Poiseuille flow, the two-dimensional lid-driven cavity flow, and the three-dimensional lid-driven cavity flow are carried out. The accuracy, convergence and robustness of the proposed method is demonstrated by comparing the computational results with analytical solution or reference data in literature. And some benchmark solutions for the three-dimensional lid-driven cavity flow of power-law fluids are provided by the validated method.

**Plain Poiseuille flow**

The proposed method is first tested on the plain Poiseuille flow of non-Newtonian power-law fluids. The physical configuration of this example is the flow between two parallel plates respectively placed at  $y=\pm H/2$ . The flow is driven by a constant pressure gradient  $\partial p/\partial x$  along the streamwise direction and would exhibit a unidirectional velocity profile along the transverse direction at the steady state, which gives

$$u(y) = \frac{n}{n+1} \left[ -\frac{1}{\mu_0} \frac{\partial p}{\partial x} \right]^{1/n} \left[ \left[ \frac{H}{2} \right]^{1+1/n} - |y|^{1+1/n} \right] \quad (2.14)$$

And the maximum velocity is

$$u_{max} = \frac{n}{n+1} \left[ -\frac{1}{\mu_0} \frac{\partial p}{\partial x} \right]^{1/n} \left[ \frac{H}{2} \right]^{1+1/n} \quad (2.15)$$

Numerical simulations are carried out on the uniform mesh size of  $41 \times 41$ , and various power law indexes of  $n=0.25, 0.5, 1.0, 1.5$  and  $2.0$  are considered. Specifically, no-slip boundary condition is implemented on the upper and lower walls, while periodic boundary condition is adopted on the inlet and outlet boundaries. Computational results are presented in Figure 1 and compared with the analytical solutions. The good agreements between the analytical and the numerical solutions at different power law indexes provide initial validation of the accuracy of the proposed SLBM for non-Newtonian power-law fluids. However, this example essentially reflects a one-dimensional fluid behaviour; validations on more complex problems are necessary

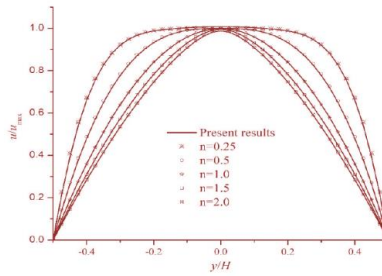


**Figure 2.1 Velocity profile of plain Poiseuille flow for non-Newtonian power-law fluid. The solid lines represent the present results, while the scattered points denote analytical solutions.**

**Two-Dimensional Lid-Driven Cavity Flow**

The two-dimensional lid-driven cavity flow has been a widely used benchmark test for numerical schemes. In this subsection, we use this problem to further validate the accuracy and robustness of SLBM. The lid-driven cavity flow refers to the fluid system in a square cavity with its top lid moving at a constant velocity  $U_0$ . As a typical internal viscous flow, solutions to this problem are characterized by the Reynolds number. Specifically, for non-Newtonian power-law fluid, the Reynolds number is defined as

$$Re = \frac{\rho U_0^{2-n} L^n}{\mu_0} \quad (2.16)$$

Where  $L$  is the length of the square cavity

To reveal the non-Newtonian behaviors, we consider two different power indexes of  $0.5$  and  $1.5$ , which respectively corresponds to the shear-thinning and shear-thickening fluids. For this example, the effect of the moving lid is transmitted through the shear forces within the boundary layers. The shear-thinning fluid would further reduce the physical viscosity within the boundary layer, which yields thinner boundary layer and higher velocity gradient near the top lid. Such flow characteristic

would pose extra difficulty to numerical simulations. Therefore, the mesh resolutions adopted in our simulations aim to capture the sharp velocity gradient changes in the shear-thinning cases.

Simulations are first conducted on uniform mesh sizes of  $201 \times 201$  for cases at low Reynolds numbers of  $100$  and  $500$ . The velocity profiles along the centerlines are plotted in Figure 2 and compared with reference values in literature [14, 36]. Note that the velocity and the physical location are normalized by the  $U_0$  and  $L$ , respectively. The computational results obtained by SLBM agree well with the reference data, which validates its accuracy for this example. Specifically, as shown in the U-Y curves, the velocity gradient near the top lid in the case of  $n=0.5$  is significantly larger than the gradient in the case of  $n=1.5$ . This can be explained by the shear-thinning behavior mentioned above.

At higher Reynolds numbers, velocity gradients near the boundaries would be further enlarged. Therefore, the non-uniform meshes are preferred in such circumstances. The implementation of SLBM on non-uniform meshes relies on appropriate interpolation algorithm to determine the physical properties at streaming nodes. In the present study, we adopt the

three-point Lagrange interpolation algorithm whose effectiveness has been validated in previous tests of Newtonian flows [37]. Validation is performed in the case of  $Re=5000$  on non-uniform mesh size of  $201 \times 201$ , and the velocity profiles along centerlines are presented in Figure 3. The good agreement between our numerical results and the reference data [15, 38] demonstrates the correctness of our implementation on non-uniform meshes and the validity of SLBM at higher Reynolds numbers. Also enclosed in Figure 3 are the convergence test and benchmark solution at  $Re=7500$ . Here we adopted four sets of mesh sizes, i.e.  $41 \times 41$ ,  $201 \times 201$ ,  $301 \times 301$  and  $401 \times 401$ , in numerical simulations. The computational results in the last three sets of meshes are quite close, which proves the convergence of SLBM at this Reynolds number. Given its validated accuracy and robustness in previous cases, numerical results in the finest mesh size can be referred as the benchmark solution to the problem at  $Re=7500$ . Another interesting point is that smooth velocity profiles are obtained on the coarse mesh size of  $41 \times 41$ . For conventional LBM, it is quite challenging to give stable solution on such mesh size at high Reynolds numbers. And the smallest relaxation parameter in this particular case reads  $\tau_{min}=0.500001$ , which is very much likely to induce

numerical instability for conventional LBM [23]. Such performance suggests that the present simplified lattice Boltzmann method bears better numerical stability than conventional LB models.

Streamlines at different Reynolds numbers and power law indexes are shown in Figure 4. The smoothness of the streamlines indicates the numerical stability of SLBM in simulating non-Newtonian power-law fluid flows. It is also noted that the shear-thickening fluid ( $n=1.5$ ) is more likely to trigger secondary minor vortices than the shear-thinning fluid ( $n=0.5$ ) at the right-bottom corner. This is caused by the stagnation point at the right-bottom corner which induces small shear rates nearby. For shear-thickening fluid, the small shear rates would reduce the physical viscosity and thus stimulates the generation of minor vortices. The shear-thinning fluid, on the contrary, exhibits large physical viscosity at small shear rates, which hinders the emerging of minor vortices. Quantitative comparisons of the location of the primary vortex for shear-thinning cases are carried out in Table 2. Good agreement between the present results and the reference data [15] further validates the accuracy of the proposed method in this test example .

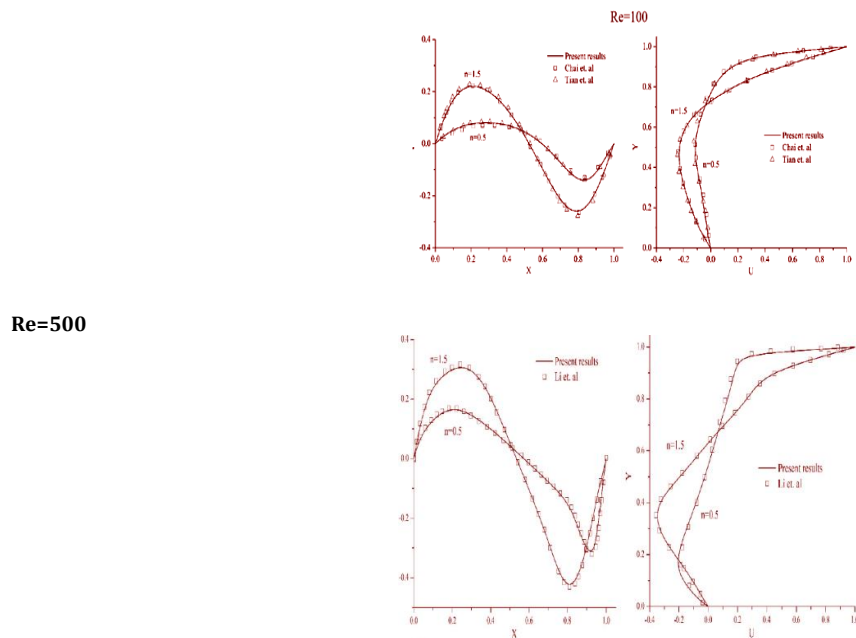
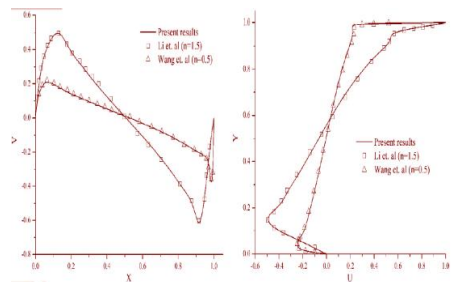


Figure 2.2 Velocity profiles along centerlines in 2D lid-driven cavity flow for non-Newtonian power-law fluid at  $Re=100$  and  $500$ . Left: X-V curve; right: U-Y curve.

Re=5000



Re=7500

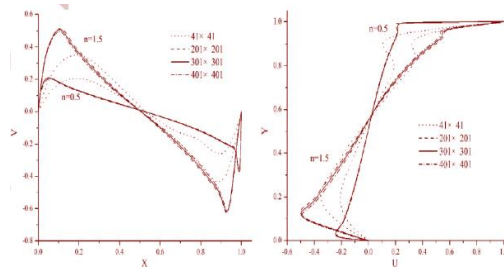


Figure 2.3 Velocity profiles along centerlines in 2D lid-driven cavity flow for non-Newtonian power-law fluid at Re=5000 and 7500. Left: X-V curve; right: U-Y curve.

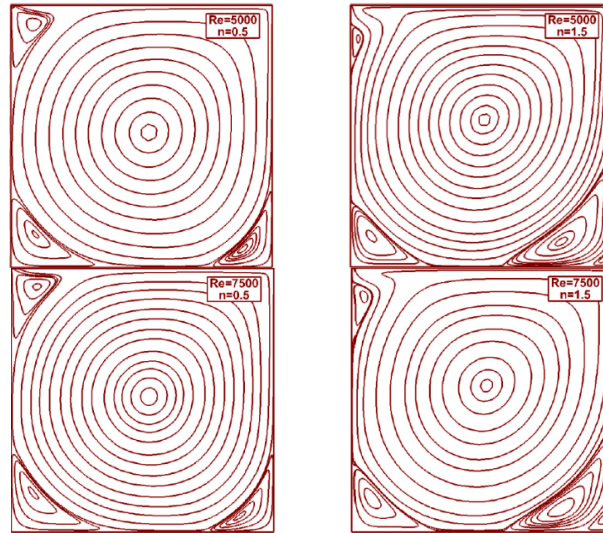


Figure 2.4 streamlines of the 2D lid-driven cavity flow for non-Newtonian power-law fluid.

Table 2.2 Comparisons of the location of the primary vortex in lid-driven cavity flow of non-Newtonian power-law fluids with  $n=0.5$ .

	Re=100	Re=500	Re=5000	Re=7500
Present	0.7118	0.5697	0.5282	0.5259
Li et al. [15]	0.7168	0.5793	0.5255	-
Present	0.7815	0.5501	0.5131	0.5125
Li et al. [15]	0.7826	0.5497	0.5190	-

**Three-dimensional lid-driven cavity flow**

Although numerical examples of two-dimensional non-Newtonian power-law fluids are abundant in literature, relative studies in three-dimensional scenario remain scarce. In this subsection, we present the computational results of SLBM for three-dimensional lid-driven cavity flow. Similar to the two-dimensional lid-driven cavity flow, solutions to this three-dimensional problem are also determined by the Reynolds number defined in Eq. (33). Since the accuracy and robustness of SLBM have been validated in previous examples, here we aim to provide converged solutions at various Reynolds numbers. These converged solutions could be utilized as benchmark results in future studies.

Three different Reynolds numbers of 400, 1000 and 1500 are considered here. Two power law indexes of  $n=0.5$  and  $1.5$ , which respectively correspond to the shear-thinning and shear-thickening flows, are studied. The computational domain is illustrated in Figure 5, and convergence tests are carried out in a

series of non-uniform mesh sizes of 613, 813, 1013, and 1213. Figure 6 and Figure 7 present velocity profiles along the centerlines in cases with  $n=0.5$  and  $1.5$ , respectively. For cases of  $Re=400$  and  $1000$ , little variation of velocity profile is observed when the mesh size is finer than 813. And for the case of  $Re=1500$ , convergence is achieved at the finer mesh size of 1013. Specifically, the converged results reveal larger velocity gradients near the top lid in shear-thinning scenario, which is consistent to the flow characteristics reflected in the two-dimensional simulations as shown in Section 4.2.

To further illustrate the physical flow pattern, streamlines on the mid-plane of  $y=0.5$  are shown in Figure 8. It is noted that the streamlines are more squeezed to the top lid in shear-thinning fluid ( $n=0.5$ ) due to the high velocity gradient, which is consistent to the velocity profile presented in Figure 6. The emerging of minor vortices at the bottom corners is more stimulated in the shear-thickening scenario ( $n=1.5$ ), which can be explained by reduced physical viscosity at lower shear rate in

such condition. In general, the numerical results fulfil the expectation and can be well explained from the physical perspective .

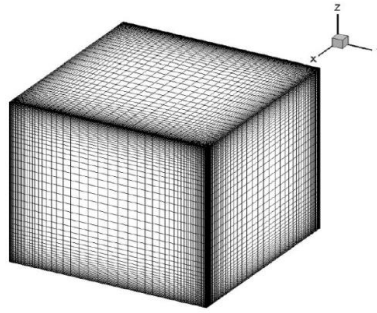


Figure 2.5 Illustration of the computational domain of three-dimensional lid-driven cavity flow of non-Newtonian power law fluid.

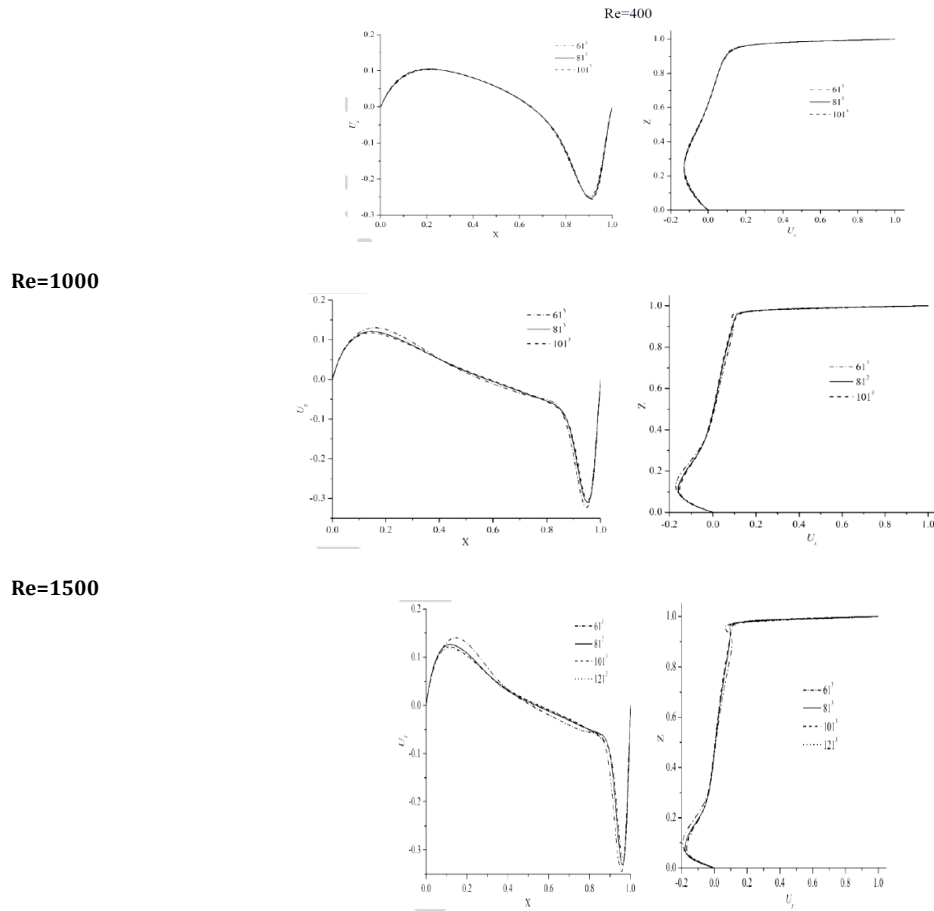
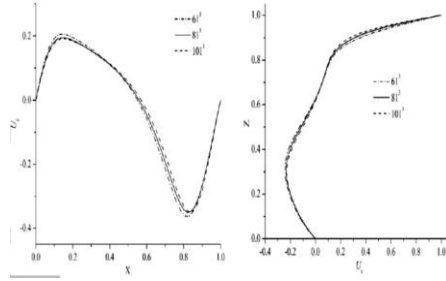


Figure 2.6 Velocity distributions along the centerlines in 3D lid-driven cavity flow for non-Newtonian power-law fluid with  $n=0.5$ . Left: X- $U_x$  curve; right:  $U_x$ -Z curve.

Re=400

Re=1000



Re=1500

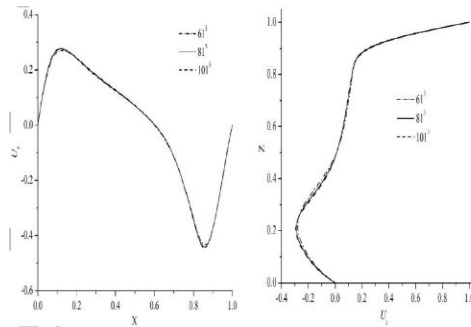
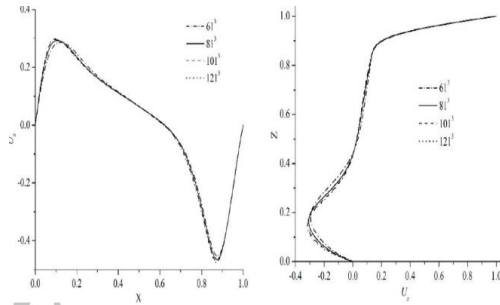
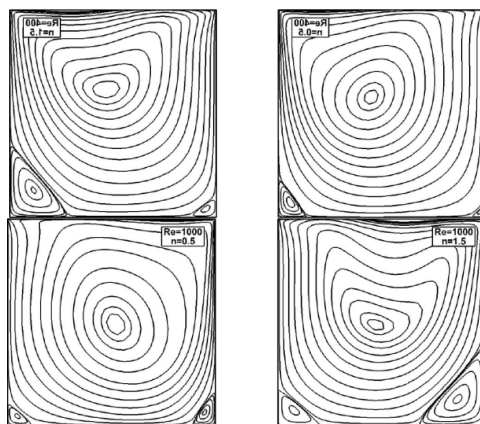


Figure 2.7 Velocity distributions along the centerlines in 3D lid-driven cavity flow for non-Newtonian power-law fluid with  $n=1.5$ . Left: X-Uz curve; right: Ux-Z curve.



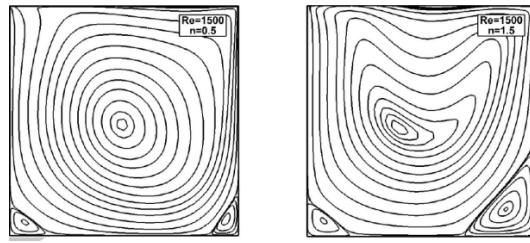


Figure 2.8 Streamlines on the plane of  $y=0.5$  in 3D lid-driven cavity flow for non-Newtonian power-law fluid.

### NON-NEWTONIAN FLUID MATHEMATICA

In this work study four non-Newtonian fluid mechanics problems using Mathematica. Constitutive equations describing the behaviour of power-law, Bingham and Carreau models are recalled. The velocity profile is obtained for the horizontal flow of power-law fluids in pipes and annuli. For the vertical laminar film flow of a Bingham fluid we determine the velocity profile. Both problems involve the use of the shooting techniques because they have split boundary conditions. Since Mathematica® permits symbolic computations, we determine analytical expressions of volumetric flow rates for pipe flow of the Bingham and power-law fluids. We use the built-in optimization command of Mathematica, FindMinimum, in order to find the non-Newtonian fluid model from representative data of flow rates measured under different applied pressure gradients in a horizontal pipe. These pedagogic problems are used to introduce the field of non-Newtonian fluid mechanics to students at the National Institute of Applied Sciences in Tunis. The Mathematica notebooks are available from the corresponding author upon request or at Wolfram Research1.

### INTRODUCTION

A non-Newtonian fluid has a viscosity that changes with the applied shear force. These fluids are characterized by measuring or computing several rheological properties such as the viscosity and the first and second normal stresses. Rheometers are used, under oscillatory shear flow or extensional flow, to obtain experimental values of these rheological properties while kinetic theory calculations using dumbbells allow the prediction of these rheological properties. For a Newtonian fluid (such as water), the viscosity is independent of how fast you are stirring it, but for a non-Newtonian fluid it is dependent. It gets easier or harder to stir faster for different types of non-Newtonian fluids. By adding corn starch to water, one obtains a non-Newtonian fluid. Applying agitation with a spoon makes the fluid behave like a solid. Thus, the shear-thickening property of this non-Newtonian fluid becomes apparent. When agitation is stopped and the fluid is allowed to rest for a certain period of time, it recovers its liquid-like behaviour.

Many peculiar phenomena are observed with non-Newtonian fluids and constitute "fun" experiments that students can perform in the laboratory. They include dye swelling and rod climbing as well as the behavior of suspensions of particles moving in non-Newtonian versus Newtonian fluids. Students can determine the terminal fall velocity and rotation direction of a single settling particle as well as wall effects and interaction between particles. Problems involving non-Newtonian fluid flow are ubiquitous in modern industry, such as in polymer processing plants. The study of body fluids such as blood, which are non-Newtonian, has important applications in biomedical engineering. In the present paper, we show how one can use the mathematical software, Mathematica®, to solve some simple non-Newtonian fluid problems. The most relevant Mathematica® commands are inserted in the text and can be found in the any introductory book such as Mathematica®, A System for doing Mathematics by Computer by Stephen

Wolfram2. We start by reminding the reader of the few simple constitutive equations for the power-law, Carreau and Bingham fluids. Then, we give the velocity profile for the horizontal flow of power-law and Carreau fluids in a pipe and an annulus. The velocity profile for the fall of a Bingham liquid film is obtained in the next section. We also derive volumetric flow rate expressions for pipe flow of Bingham and power-law fluids. In the last part of the paper, we make a model determination using the previously found volumetric flow rate expressions and representative data.

### Constitutive equations for non-Newtonian fluids

For Newtonian fluids, the shear stress,  $\tau$ , is proportional to the strain rate,  $\dot{\gamma}$

$$\tau = \eta \dot{\gamma} \quad (3.1)$$

where the viscosity,  $\eta$ , the proportionality factor, is constant. The situation is different for non-Newtonian fluids and the viscosity is a function of the strain rate:

$$\tau = \eta[\dot{\gamma}] \dot{\gamma} \quad (3.2)$$

Different constitutive equations, giving rise to various models of non-Newtonian fluids, have been proposed in order to express the viscosity as a function of the strain rate. In power-law fluids, the following relation is satisfied:

$$\eta = \kappa \dot{\gamma}^{n-1} \quad (3.3)$$

Dilatant fluids correspond to the case where the exponent in equation (3) is positive ( $n > 1$ ) while pseudo-plastic fluids are obtained when  $n < 1$ . We see that viscosity decreases with strain rate for  $n < 1$ , which is the case for pseudo-plastic fluids, also called shear-thinning fluids. On the other hand, dilatant fluids are shear-thickening. If  $n = 1$ , one recovers the Newtonian fluid behavior.

The Carreau model describes fluids for which the viscosity presents a plateau at low and high shear rates separated by a shear-thinning region:

$$\frac{\eta - \eta_{\infty}}{\eta_0 - \eta_{\infty}} = \frac{1}{[1 + (\lambda \dot{\gamma})^2]^{(1-n)/2}} \quad (3.4)$$

where  $\eta_0$  is the zero-shear viscosity and  $\eta_{\infty}$  is the infinite-shear viscosity. Finally, the Bingham model is defined as follows:

$$\text{At low shear rates: } \frac{1}{2} (\tau : \tau) \leq \tau_0^2, \quad \dot{\gamma} = 0 \quad (3.5)$$

$$\text{At high shear rates: } \frac{1}{2} (\tau : \tau) > \tau_0^2, \quad \tau = \left[ \eta + \frac{\tau_0}{\dot{\gamma}} \right] \dot{\gamma} \quad (3.6)$$

### Horizontal Flow of Carreau and Power-Law Fluids in a Pipe

Find the velocity profiles for the laminar flow of power-law and Carreau fluids in a pipe, shown in Fig. 1. Use the following values for the pressure difference  $\Delta p$ , the exponent  $n$ , the Newtonian fluid viscosity  $\eta$ , the consistency index  $\kappa$ , the infinite-shear viscosity  $\eta_{\infty}$ , the zero-shear viscosity  $\eta_0$ , the relaxation

parameter  $\lambda$ , the pipe length  $L$  and radius  $R$ , whose units appear under "Nomenclature" at the end of this article:

**Problem statement.**

$\Delta P = 100$ ;  $L = 50$  and  $R = 0.02$

Newtonian fluid:  $\eta = 8.9 \times 10^{-4}$ .

Dilatant fluid :  $n = 3.39$  and  $k = 10^{-6}$ .

Pseudo-plastic fluid:  $n = 0.4$  and  $k = 5 \times 10^{-3}$ .

Carreau fluid:  $n = 0.5$ ,  $\lambda = 0.2$ ,  $\eta_0 = 1.72 \times 10^{-3}$  and  $\eta_\infty = 0$ .

**Solution.**

This problem is treated using Polymath®, a numerical computational package<sup>3</sup>, in the Problem Solving in Chemical Engineering with Numerical Methods by Cutlip and Shacham<sup>4</sup>. The governing equation is the z-component of the equation of motion in cylindrical coordinates:

$$\frac{1}{r} \frac{d}{dr} \left[ r k \left[ - \frac{dv_z}{dr} \right]^n \right] = \frac{\Delta P}{L} \quad (3.7)$$

Equation (7) is subject to the following split boundary conditions:

$$\text{At } r = 0: \quad \tau_{rz} = 0 \quad (3.8)$$

$$\text{At } r = R: v_z = 0 \quad (3.9)$$

These kinds of mathematical problems often require the utilization of a particular numerical approach called the shooting technique. This method consists of guessing different values of  $v$  at  $r = 0$ , solving the differential equation and checking that the no-slip boundary condition at  $r = R$  is satisfied. An analytical solution is possible for power-law fluids and details about its derivation can be found in Fluid Mechanics for Chemical Engineers by Wilkes<sup>5</sup>:

$$v_z(r) = \left[ \frac{\Delta P}{L} \frac{1}{2k} \right]^{1/n} \frac{(R^{1+1/n} - r^{1+1/n})}{1+1/n} \quad (3.10)$$

For the Carreau fluid, one must use a numerical approach since no analytical solution is available.

For the power-law fluids, the following Mathematica® commands are used to find the velocity:

System [Ω\_] = {D [τ<sub>rz</sub>[r], {r, 1}] = Δp / L r,

D [v<sub>z</sub>[r], {r, 1}] = If [τ<sub>rz</sub>[r] ≥ 0, -(τ<sub>rz</sub>[r] / x)^(1/n),

The graphical capability of Mathematica allows the student to plot the velocity profile without having to use different software. Figure 2 shows the velocity profile for the Newtonian, dilatant, Carreau and pseudo-plastic cases using the commands:

These profiles are obtained under the equal volumetric flow conditions. The velocity near the wall is higher for the Carreau and pseudo-plastic fluids than for the Newtonian and dilatant fluids. This results in higher heat transfer rates due a higher convection. The author's opinion is that the approach to solve split boundary problems using Mathematica® is more systematic than the one proposed by Cutlip and Shacham<sup>4</sup> using Polymath® despite a steeper initial learning curve for the students. In fact, it automatically finds the velocity at the center of the pipe by verifying the no-slip boundary condition and using the Mathematica® command FindRoot.

**Horizontal Flow of a Carreau and a Power-Law Fluid in an annulus**

**Problem statement**

Find the velocity profiles for the laminar flow of a power-law and Carreau fluids in an annulus, shown in Fig. 3. Use the following

values, where  $1 \leq R_1$  and  $R_2$  are the inner and outer radii, and all other symbols have already been defined:

$\Delta P = 100$ ;  $L = 50$ ;  $R_1 = 0.02$  and  $R_2 = 0.05$

Newtonian fluid:  $4.89 \times 10^{-4}$ .

Dilatant fluid:  $n = 1.2$  and  $k = 4.7 \times 10^{-4}$ .

Pseudo-plastic fluid:  $n = 0.5$  and  $k = 4.5 \times 10^{-3}$ .

Carreau fluid:  $n = 0.5$ ,  $\lambda = 0.2$ ,  $\eta_0 = 2.04 \times 10^{-3}$  and  $\eta_\infty = 0$ .

**Solution**

Cutlip and Shacham<sup>4</sup> have solved this example using Polymath®. The governing equation is again the z-component of the equation of motion in cylindrical coordinates:

$$\frac{1}{r} \frac{d}{dr} \left[ r k \left[ - \frac{dv_z}{dr} \right]^n \right] = \frac{\Delta P}{L} \quad (3.11)$$

Equation (11) is subject to the following split boundary conditions:

$$\text{At } r = R_1: \quad v_z = 0 \quad (3.12)$$

$$\text{At } r = R_2: \quad v_z = 0 \quad (3.13)$$

To solve this problem, we make use of the shooting technique in a similar fashion as the previous example. This method consists of guessing different values of  $\tau_{rz}$  at  $r = R_1$  solving the differential equation and checking that the no-slip boundary condition at  $r = R_2$  is satisfied. An analytical solution<sup>4</sup> is available for the Newtonian fluid case:

$$v_z(r) = \left[ \frac{\Delta P}{4\eta L} \right] \left[ R_2^2 - r^2 + \frac{R_2^2 - R_1^2}{\ln(R_2/R_1)} \ln(r/R_2) \right] \quad (3.14)$$

No analytical solution is available for dilatant, pseudo-plastic and Carreau fluids and one must resort to a numerical method.

For the power-law fluids, the following Mathematica® command is used to find the velocity as a function of  $r$ :

```
system[Ω_] = {D[τrz[r], {r, 1}] = ΔP / L r,
D[vz[r], {r, 1}] = If[τrz[r] ≥ 0, -(τrz[r] / x)^(1/n), (-τrz[r] / x)^(1/n),
τrz[R1] = 0, vz[R2] = 0};
myODEsoln[Ω_] := NDSolve[system[Ω], {vz, τrz}, {r, R1, R2}];
yend[Ω_?NumericQ] := Flatten[{vz[r] /. myODEsoln[Ω]} /. r -> R2];
bc = FindRoot[yend[Ω] = 0, {Ω, -2, 2}][[1, 2]];
```

One can plot the velocity profile, shown in Figure 4, for the Newtonian, dilatant, Carreau and pseudo-plastic cases using the Mathematica commands:

```
sol1 = myODEsoln[bc];
plt1 = Plot[vz[r] /. sol1, {r, 0.00001, R}, PlotStyle -> RGBColor[0, 0, 1]]
```

These profiles are obtained under equal volumetric flow conditions. The velocity profiles found, for all four fluids, are not symmetric. In fact, they reach a maximum value close to the radial position given by  $r = 0.033$ , slightly less than half-way from  $R_1$  and  $R_2$ .

**Vertical Laminar Flow Of A Bingham Liquid Film**  
**Problem statement**

Find the velocity profile for the vertical laminar flow of a Bingham fluid down the wall depicted in Figure 5. Values of the gravitational acceleration,  $g$ , the density,  $\rho$ , the yield stress,  $\tau_0$ , the zero-shear viscosity,  $\eta_0$ , the film thickness,  $\delta$ , are given by:

$$g = 9.81; \rho = 950; \tau_0 = 5; \eta_0 = 0.15 \text{ and } \delta = 0.005$$

**Solution.**

Cutlip and Shacham<sup>4</sup> have presented a solution of this example using Polymath<sup>®</sup>. The governing equation is the z-component of the equation of motion in rectangular coordinates:

$$\frac{d\tau_{xz}}{dx} = \rho g \quad (3.15)$$

Equation (15) is subject to the following split boundary conditions:

$$\text{At } x = 0: \tau_{xz} = 0 \quad (3.16)$$

$$\text{At } x = \delta: v_z = 0 \quad (3.17)$$

We make the same treatment as the first two problems by applying the shooting technique:

```

system[Ω] := {D[τxz[x], {x, 1}] == ρ g,
D[vz[x], {x, 1}] == If[Abs[τxz[x]] ≤ τ0, 0,
If[τxz[x] > τ0, (τ0 - τxz[x]) / η0, -(τ0 + τxz[x]) / η0}], τxz[0] == 0, vz[0] == Ω};
myODEsoln[Ω] := NDSolve[system[Ω], {vz, τxz}, {x, 0, δ}];
yend[Ω_?NumericQ] := Flatten[{vz[x] /. myODEsoln[Ω]} /. x -> δ];
bc = FindRoot[yend[Ω] == 0, {Ω, 0, 0.5}][[1, 2]];
    
```

For the Newtonian case, an analytical expression for the velocity,  $v_z$ , as a function of position,  $x$ , can be easily derived:

$$v_z = \frac{\rho g \delta^2}{2\eta} \left[ 1 - \left( \frac{x}{\delta} \right)^2 \right] \quad (3.18)$$

In Figure 6, we show the velocity profile for the Newtonian and the Bingham fluids. This plot is obtained by using the Mathematical commands :

```

sol1 = myODEsoln[bc]
plt1 = Plot[vz[x] /. sol1, {x, 0, δ}, PlotStyle -> RGBColor[0, 0, 1]]
    
```

A comparison of the velocity profile obtained using the analytical solution for the Newtonian fluid and the velocity profile corresponding to the Bingham fluid shows that the latter is flat near the surface of the liquid film. In fact, we have a non-zero velocity gradient only when  $\tau_{xz} > \tau_0$ . This behavior is typical of Bingham fluids.

**Expressions of Volumetric Flow Rates**
**Problem statement**

Derive expressions of volumetric flow rates for pipe flow of Bingham and power-law fluids using symbolic computations with Mathematica<sup>®</sup>.

**Solution.**
**Power-Law Fluid Case**

First, we find the expression of the shear stress,  $\tau_{rz}$ , as a function of the radial position,  $r$ :

```

sol3 = DSolve[D[r τrz[r], {r, 1}] == -ΔP / L r, τrz[r], r]
τrz[r] = sol3[[1, 1, 2]] /. C[1] -> 0
    
```

We get the following result:

$$\tau_{rz} = -\frac{\Delta P r}{2L} \quad (3.19)$$

Then, we determine the velocity distribution using the symbolic command, Solve,

```

sol4 = DSolve[D[vz[r], {r, 1}] == -(τrz[r] / κ)^(1/n), vz[r], r]
vz[r] = sol4[[1, 1, 2]] /. C[1] -> \frac{2^{-1/n} n R \left(\frac{\Delta P R}{\kappa L}\right)^{1/n}}{1+n}
    
```

Finally, the symbolic command, Integrate, is used,

```
Q = Integrate[2 Pi r vz[r], {r, 0, R}]
```

And we get the following expression for the volumetric flow rate,

$$Q = \frac{2^{-1/n} n R^3 n \left(\frac{\Delta P R}{\kappa L}\right)^{1/n}}{1+3n} \quad (3.20)$$

**Bingham fluid case**

Just like the treatment above, we start by finding the expression of the shear stress,  $\tau_{rz}$  as a function of the radial position,  $r$ :

```
So11 = DSolve[D[r τrz[r], {r, 1}] == -ΔP / L r, τrz[r], r]
```

```
τrz[r] = so11[[1, 1, 2]] /. C[1] -> 0
```

We get the following result :

$$\tau_{rz} = -\frac{\Delta P r}{2L} \quad (3.21)$$

In the first part of the derivation, we determine the velocity distribution between  $r = (2\tau_0 L) / \Delta p$  and  $r = R$  using boundary condition  $v_z(R) = 0$  and the symbolic command, Dsolve:

```
So12 = DSolve[D[vz[r], {r, 1}] == (τrz[r] + τ0) / η, vz[r], r]
```

```
vz[r] = so12[[1, 1, 2]] /. C[1] -> \frac{\Delta P R^2}{4\eta L} - \frac{R\tau_0}{\eta}
```

The symbolic command, Integrate, is used to obtain the expression of the volumetric flow rate between  $r = (2\tau_0 L) / \Delta p$  and  $r = R$ ,

```
Q1 = Integrate[2 Pi r vz[r], {r, \frac{2\tau_0 L}{\Delta P}, R}]
```

In the second part of the derivation, we determine the constant velocity,  $v_0$ , between  $r = 0$  and  $r = (2\tau_0 L) / \Delta p$  using the following symbolic command:

```
v0 = 1 / μ P G (r^2 - R^2) / 4 + τ0 / μ (r, R) /. r -> 2 τ0 L / ΔP
```

This is nothing more than expressing the continuity of the velocity at  $r = (2\tau_0 L) / \Delta p$ . In fact, we have written that  $v_0 = v_z(2\tau_0 L) / \Delta p$  in the Mathematica<sup>®</sup> statement.

The symbolic command, Integrate, is used to obtain the expression of the volumetric flow rate between  $r = 0$  and  $r = (2\tau_0 L) / \Delta p$ ,

$$Q_2 = \text{Integrate} [2 \text{ Pi } r v_0, \{r, 0, 2 \tau_0 L / \Delta P\}]$$

and we get the following expression for the overall volumetric flow rate,

$$Q = \frac{\pi R^4 \Delta P}{8 \eta L} - \frac{\pi R^3 \tau_0}{3 \eta} + \frac{2 \pi \tau_0^4 L^3}{3 \eta \Delta P^3} \quad (3.22)$$

**Non-Newtonian fluid model determination**

**Problem statement.**

Wilkes5 provides representative values of the volumetric flow rate versus the applied pressure gradient for horizontal flow in a pipe. These values are reproduced in Table 1. The pipe radius is equal to  $m R = 0.01$ . Use these representative values, in conjunction with the analytical expression of the volumetric flow rates determined in the previous section, to compute the parameters of the constitutive equation.

**Solution**

First, we compute the following sum:

$$J = \sum_{i=1}^{10} (Q_i^{\text{rep}} - Q_i^{\text{th}})^2 \quad (3.23)$$

**RESULTS**

Where  $Q_1^{\text{rep}}$  and  $Q_1^{\text{th}}$  are the representative value and analytical expression of the volumetric flow rate? Then, we use the built-in command of Mathematical, FindMinimum, to determine the values of  $n$  and  $k$  for the power-law model and  $\tau$  and  $\eta$  for the Bingham model that minimize the objective function  $J$ . The approach use here is the least squares method. For the power-law model, we find  $n = 0.437$  and  $k = 6.708$  while for the Bingham model the result is  $\tau_0 = 77.55$  and  $\eta = 0.0326$ . The value of the sum given by equation (22) is  $9.89 \times 10^{-6}$  for the Bingham model and  $2.67 \times 10^{-7}$  for the power-law model. Thus, we conclude that the power-law model fits the representative data better

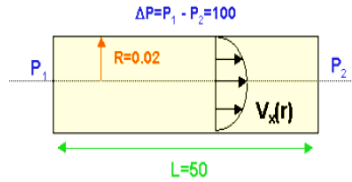


Figure: 3.1

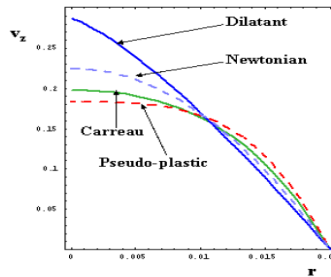


Figure: 3.2

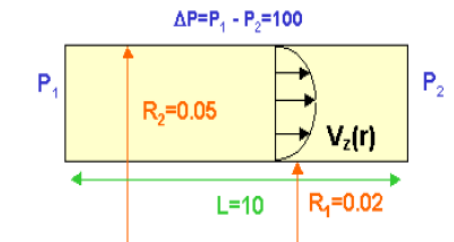


Figure: 3.3

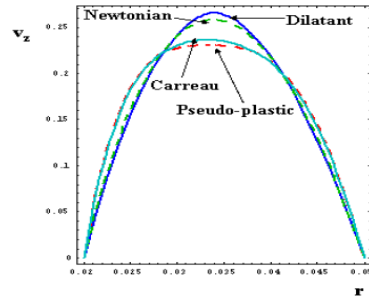


Figure: 3.4

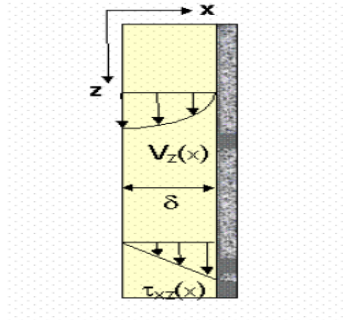


Figure: 3.5

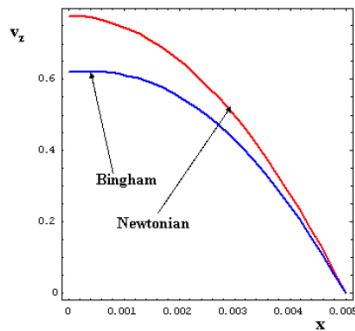


Figure: 3.6

Table: 3.1

$\Delta P/L$ (Pa/m)	$10^5 \times Q$ ( $m^3/s$ )
10000	5.37
20000	26.4
30000	68.9
40000	129
50000	235
60000	336
70000	487
80000	713
90000	912
100000	1100

**CONCLUSIONS**

A simplified lattice Boltzmann method for non-Newtonian power-law fluid flows is proposed in this paper. This method extracts the idea of its Newtonian counterpart, and reconstructs solutions to the macroscopic equations recovered from the lattice Boltzmann equation through the Chapman-Enskog expansion analysis. The reconstruction process follows a predictor-corrector manner and utilizes isentropic properties and relationships given in the Chapman-Enskog expansion

analysis. To model the non-Newtonian behaviors in which the physical viscosity varies in the space, a truncated power-law model is incorporated to locally adjust the relaxation parameter in the method. Compared with other non-Newtonian lattice Boltzmann models, the present one tracks the evolution of macroscopic variables instead of distribution functions, which reduces the cost of virtual memory and facilitates implementation of physical boundary conditions.

The accuracy and robustness of the proposed method is validated by two examples of the plain Poiseuille flow and two-dimensional lid-driven cavity flow with power-law fluids. Further tests on three-dimensional lid-driven cavity flow of shear-thinning and shear-thickening fluids are then carried out, which validates the convergence of the method and provides benchmark solutions for future reference

**BOUNDARY LAYER FLOW NON-NEWTONIAN FLUIDS**

The investigation of boundary layer flow along surfaces embedded in fluid saturated porous media has received considerable interest recently, especially in the enhanced recovery of petroleum resources, packed bed reactors and geothermal industries. Considerable attention has been directed toward understanding the transport properties of porous media subjected to heat transfer [1]-[3]. Non-Newtonian fluids generally do not follow the linear relation between shear stress and shear strain rate. These fluids may be classified as inelastic and viscoelastic. In addition, the Ostwald-de Waele power-law model represents several inelastic time-independent non-Newtonian fluids of practical interest (Barnes et al. [4]). These fluids can be divided into four groups: pseudo-plastic, dilatant, ideal Bingham plastic and plastic. A dilatant, or shear-thickening, fluid increases resistance with increasing applied stress. Alternately, a pseudo-plastic, or shearthinning, fluid decreases resistance with increasing stress [5].

**INTRODUCTION**

Thus, the equations governing the conservation of mass, momentum and energy can be written as [9]:

$$\frac{\partial u}{\partial x} + \frac{\partial v}{\partial y} = 0 \quad (4.1)$$

$$U \frac{\partial T}{\partial x} + v \frac{\partial T}{\partial y} = -\frac{1}{p} \frac{\partial p}{\partial x} - \frac{\mu \epsilon}{pK} u^n - \frac{F \epsilon^2}{\sqrt{K}} u^2 + \frac{1}{p} \frac{\partial}{\partial y} \left[ \mu \left| \frac{\partial u}{\partial y} \right|^n \right] \quad (4.2)$$

$$U \frac{\partial T}{\partial x} + v \frac{\partial T}{\partial y} = \alpha \frac{\partial^2 T}{\partial y^2} \quad (4.3)$$

where  $u$  and  $v$  are the velocity components along the  $x$  and  $y$  directions,  $T$  is the fluid temperature,  $p$  is the density,  $n$  is the power-law index of non-Newtonian fluid,  $\alpha$  is the thermal diffusivity of the medium,  $s$  is the medium porosity,  $\mu$  is the coefficient of viscosity,  $K$  is the permeability and  $F$  is an empirical constant in the second-order resistance.

The above governing equations need to be solved subject to the following boundary conditions on velocity and temperature fields :

$$u = 0, \quad v = 0, \quad T = T_n \quad \text{on } y = 0 \quad (4.4)$$

Merkin [6] studied a similarity transformation which can deal with isothermal two-dimensional and axisymmetric bodies of arbitrary shape. Nakayama and Koyama [7] have extended Merkin's method and provided similarity solutions for the natural convection in non-Newtonian power-law fluids over bodies of arbitrary geometry placed in a porous medium. Mehta and Rao [8] have studied the steady buoyancy-induced flow of a non-Newtonian fluid in a porous medium bounded by a vertical flat plate, using Karman-Pohlhausen integral method and numerically by similarity method.

The primary purpose of the present study is to predict the characteristics of flow fields past a wedge using the model of the flow of non-Newtonian power law fluids in a porous medium given by Hady and Ibrahim [9]. The transformed boundary layer equations are solved using the fourth-order Runge-Kutta integration scheme with the Newton-Raphson shooting method. The effects of power-law non-Newtonian fluid parameter and the presence of an isotropic solid matrix on the velocity field are investigated.

**Formulation of problems**

Let us consider the two-dimensional steady flow in a porous medium saturated with power-law non-Newtonian fluids past an impermeable wedge having a small wedge angle. The physical model and geometrical coordinates are shown in Fig. 1. The  $x$ -axis is measured along the body surface from its leading edge, and  $y$ -axis normal to it. The effects of viscous dissipation will be assumed to be negligible

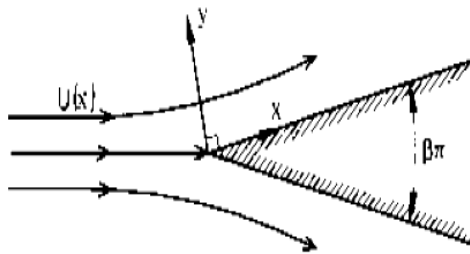


Fig. 4.1 The physical model and coordinate system

$$u \rightarrow U, \quad v \rightarrow 0, \quad T \rightarrow T_n \quad \text{as } y \rightarrow \alpha \quad (4.5)$$

Where  $U$  is the free stream velocity in this study we introduced the following transformations:

$$H = yg \quad (x) = \frac{y}{x} Re_x^{-\frac{1}{n+1}}, \Psi = U(x)x Re_x^{-\frac{1}{n+1}} f(\eta), U(x) = Cx^m$$

$$Re_x = (m + 1) \frac{\rho x^n U(x)^{2-n}}{\mu}, \theta = \frac{T - T_\alpha}{T_n - T_\alpha}, u = U(x)f'$$

$$V = -U(x) Re_x^{-\frac{1}{n-1}} \frac{1}{n+1} \{ [m(2n-1)+1]f + [m(2-n)-1]\eta f' \} \quad (4.6)$$

where a prime represents differentiation with respect to  $\eta$ ,  $Re_x$  is the Reynolds number, and the exponent  $m$  be termed the Falkner-Skan power-law parameter, and is related to the wedge angle finby [5]

$$\beta = \frac{2m}{1+m} \quad (4.7)$$

The continuity eqn (1) is automatically satisfied by a stream function  $\psi$  such that

$$U = \frac{\partial \psi}{\partial y}, \quad v = -\frac{\partial \psi}{\partial x} \quad (4.8)$$

With the aid of the above transformations, the boundary layer eqn (2) can be written as

$$n|f^m|^{n-1}f^m + \frac{m(2n-1)+1}{(m+1)(n-1)}ff^n$$

$$= -\frac{b}{m+1} + \frac{1}{m+1}(B-m)f^{-2} - \frac{A}{m+1}[1 - (f^n)^n] = 0 \quad (4.9)$$

Where

$$A = \frac{\mu \varepsilon}{\rho K} x U^{n-2} = \frac{m+1}{\text{Re}_x} \frac{x^{n+1} \varepsilon}{K}, B = \frac{F \varepsilon^2}{\sqrt{K}} x \quad (4.10)$$

If m is assumed to be zero, the above governing eqn (9) is identical to the one reported by Hady and Ibrahim [9], which represents the incompressible powerlaw non-Newtonian boundary layer flow over a flat plate.

In addition, we obtain the following ordinary differential equation governing the thermal field for the case of a constant wall temperature:

$$\theta^n + \frac{m(2n-1)+1}{n+1} \text{Pr} f \theta' = 0 \quad (4.11)$$

The boundary conditions (4) and (5) can be rewritten as

$$f = f' = 0, \quad \theta = 1 \quad \text{on } \eta = 0 \quad (4.12)$$

$$f' \rightarrow 1, \quad \theta \rightarrow 0 \quad \text{as } \eta \rightarrow x \quad (4.13)$$

The shear stress at the body surface is given by

$$\tau_n = \mu \left. \frac{\partial u}{\partial y} \right|_{y=0}^n = \mu U^n x^{-n} \text{Re}_x^{\frac{n}{n-1}} |f^n(0)|^n \quad (4.14)$$

Therefore, the local skin friction coefficient can be written as follows:

$$\frac{1}{2} C_f \text{Re}_x^{\frac{1}{n+1}} = (m+1) |f'(0)|^n \quad (4.15)$$

In addition, the local heat transfer coefficient and Nusselt number can be written by Fourier's law as

$$h_1(x) = \frac{q_w(x)}{T_u - T_s} = -k \theta'(0) \frac{1}{x} \text{Re}_x^{\frac{1}{n-1}} \quad (4.16)$$

$$\text{Nu} \text{Re}_x^{\frac{1}{n-1}} = -\theta'(0) \quad (4.17)$$

**RESULTS AND DISCUSSION**

The nonlinear ordinary differential eqns (9) and (11), satisfying the boundary conditions (12)-(13) have been solved numerically, using the fourth-order Runge-Kutta method for several values of parameters m, n, A and B.

In the present study the boundary condition for  $\eta \rightarrow x$  is replaced by where  $\eta_{max}$  is a sufficiently large value of  $\eta$  where the velocity profile u can be approached to the relevant free stream velocity. We choose  $\eta_{max} = 8$  and a step size  $\Delta \eta = 0.001$ , and four decimal accuracy as the criterion for convergence

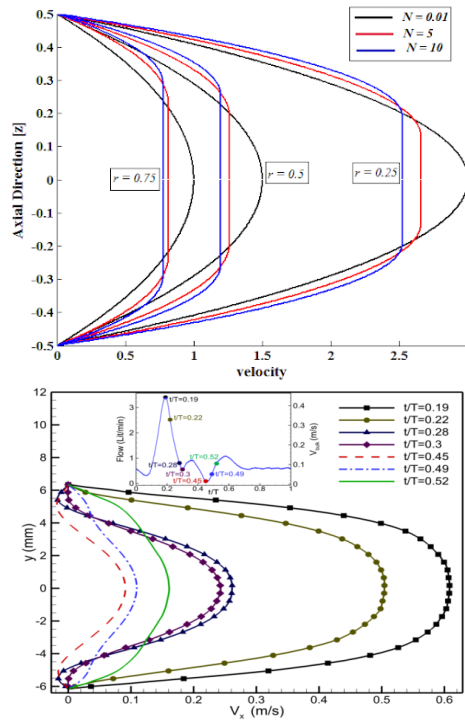


**Figure 4.2: Velocity distribution over a flat plate for various non-Newtonian fluid index parameter n with #=0.1: (a) ,4=0.1. (b) A=0.5.**

In order to assess the accuracy of the present computer simulation model, the results are compared with accepted data sets for Newtonian fluids over a wedge and the boundary layer flow of power-law non-Newtonian fluids over a flat plate corresponding to the case computed by Hady and Ibrahim [9], and showed a good agreement.

In Figures 2-5 we have shown some graphs of the flow and temperature fields of power-law non-Newtonian fluids as a

function of  $\eta$ . Slight variation of velocity distribution in the vicinity of a flat plate for the different fluid index parameter n and  $\varepsilon=0.1$  is observed in Fig. 2. The results show that for  $A=0A$  the thickness of velocity boundary layer of the pseudo- plastic fluid is higher than that of the Newtonian or dilatant fluids. However, as shown in Fig. 2(b), the velocity distribution is lower in the case of the pseudo-plastic fluid when compared with the

Newtonian fluid while the first-order resistance parameter is held constant with 0.5.

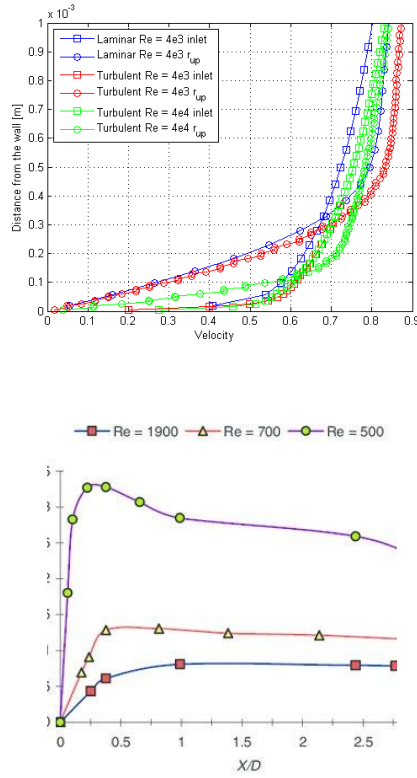


Figure 4.3: Effects of wedge angles on the velocity distribution for various non-Newtonian fluid index parameter  $n$  with,  $4=0.1$  and  $5=0.1$ .

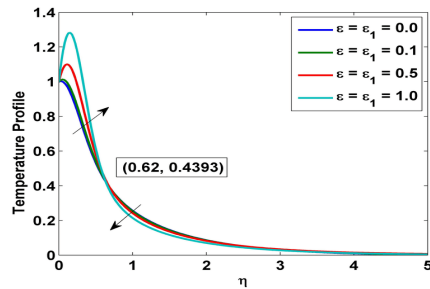
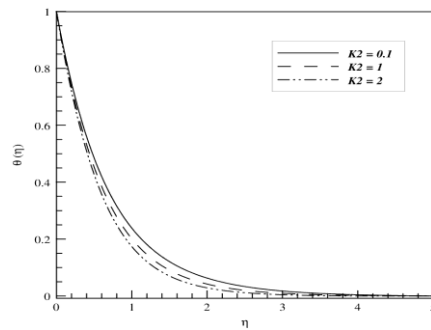


Figure 4.4: Temperature profiles over a flat plate for Newtonian fluid against spanwise coordinate  $\eta$  for different values of Prandtl number  $Pr$ .



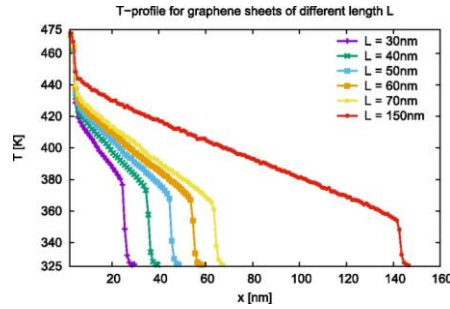


Figure 4.5: Temperature profiles against span wise coordinate  $x$  for different values of non-Newtonian fluid index  $n$  and wedge angles; (a) flat plate, (b) wedge ( $m=0.5$ ).

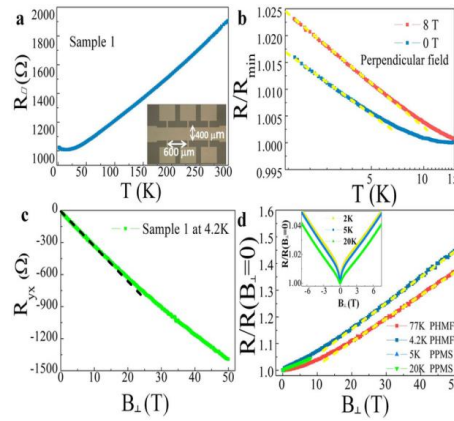


Figure 4.6 depicts the effects of wedge angles on the velocity distribution in the boundary layer for various values of fluid index  $n$  with constant resistance parameters  $A=0.1$  and  $\beta=0.1$ . It is seen that for accelerating flows ( $m, \beta > 0$ ),

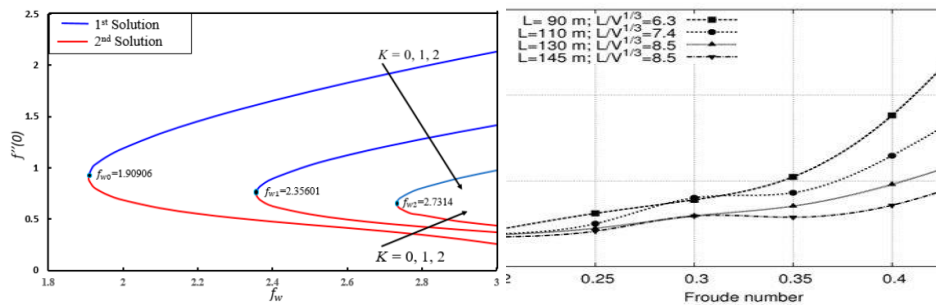
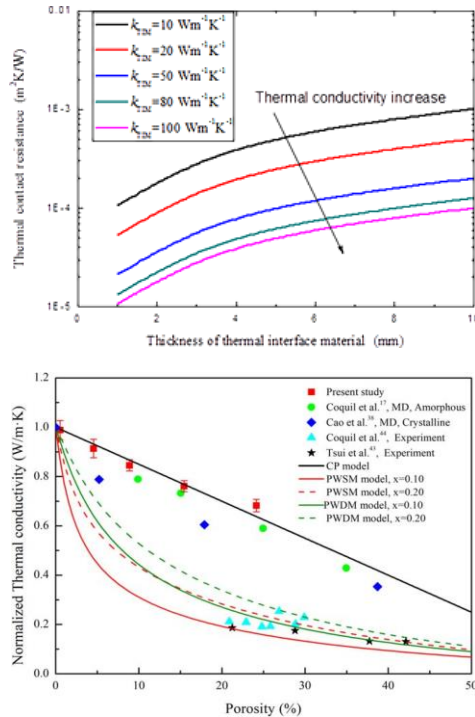


Figure 4.7: Variation of the surface skin friction factor with resistance parameters  $A$  and  $B$  for different values of the power-law index of non-Newtonian fluid  $n$ .

The peak values of velocity are larger than for a flat plate at zero incidence, and then decays to the relevant free stream velocity. Typical variations of the temperature profiles over a flat plate for Newtonian fluid ( $n=1$ ) along the span wise coordinate are shown in Fig. 4 for different values of Prandtl number  $Pr$ . The numerical results show that an increase of Prandtl number results in a decreasing thermal boundary layer thickness and more uniform temperature distribution across the boundary layer. The reason is that smaller values of  $Pr$  are equivalent to increasing thermal conductivities, and therefore heat is able to diffuse away from the heated surface more rapidly than for higher values of  $Pr$ . Hence the boundary layer is thicker and the rate of heat transfer is reduced, for gradients have been reduced.

Figure 5 displays the effects of wedge angles on the dimensionless temperature profiles for the different power-law index of non-Newtonian fluid with  $Pr=1$ ,  $A=0.1$  and  $\beta=0.1$ . These trends show that for the case of a flat plate the thickness of the thermal boundary layer is increased as the non-Newtonian fluid index parameter  $n$  increases (see Fig. 5(a)). As shown in Fig. 5(b), furthermore, the temperature profile in the vicinity of a wedge ( $m=0.5$ ) changes slightly for different values of the power-law index of non-Newtonian fluid.



**Figure 4.8: Variation of the surface heat transfer rate with resistance parameters A and B for different values of the power-law index of non-Newtonian fluid n.**

For illustrative purposes, the friction coefficient grouping  $(m+1)|f^n(1)|^m$  is presented in Fig. 6, where the abscissa variables are set to the first-order resistance parameter A and the second-order resistance parameter B, respectively, to see its effect on local skin friction coefficient for the different fluid index parameter n. As depicted in Fig. 6(a), the local skin friction coefficient is lower in the case of the dilatants fluid ( $n=2$ ) when compared with the pseudo-plastic or Newtonian fluids for the case of fixed parameters  $m=0.3$  and  $\epsilon=0.1$ . The results also show that for the case of a dilatants fluid, an increase in A leads to a drop in the values of skin friction factor first to a minimum at about  $A=0.3$ , and then increases. As shown in Fig. 6(b), the local skin friction factors of non-Newtonian fluids having different power-law index decrease initially to a minimum and then increases as the second-order resistance parameter B increases.

Figure 7 shows the variations of wedge surface heat transfer rate,  $\text{NuRe}\tau^{1/(n-1)}$ , for various resistance parameters with  $\text{Pr}=\lambda$ . The results show that an increase in the first-order resistance parameter A leads to decrease the Nusselt number. Especially, the surface heat transfer rate is lower in the case of the dilatant fluid when compared with the Newtonian or pseudo-plastic fluids while the second-order resistance parameter is held constant ( $\alpha=0.1$ ). As shown in Fig. 7(b), the variation of surface heat transfer rate for Newtonian fluid asymptotically decreases as the second-order resistance parameter B increases. However, the heat transfer rate for the pseudo-plastic and dilatants fluids decreases initially to a minimum at about  $B=0.15$  and then increases.

## CONCLUSIONS

This study gives a simple mathematical model for solving the problem of flow of non-Newtonian power-law fluids over a wedge embedded in the porous medium. Numerical results are presented to illustrate the details of the velocity and temperature fields and their dependence on the material properties of the fluid. The results for the flat plate case studied by Hady and

Ibrahim [9] correspond to the special case  $m=Q$  of the present study. It has been observed that for the constant wedge angle and fixed resistance parameters A and B, although limited considerations, the local skin friction coefficient and surface heat transfer rate are lower for a dilatant fluid, as compared with the pseudo-plastic or Newtonian fluids. For better understanding of the present work, it may be necessary to perform the experimental works.

## CONCLUSIONS

In this presented the solution of four non-Newtonian fluid mechanics problems using Mathematical. The velocity profile is obtained for the horizontal flow of power-law fluids in pipes and annuli and for the vertical laminar flow of a Bingham fluid. These problems have split boundary conditions and we applied the shooting techniques to solve them. Analytical expressions of volumetric flow rates for pipe flow of the Bingham and power-law fluids were derived using Mathematical. The parameters of the constitutive equation of non-Newtonian fluids were obtained from representative data of flow rates measured under different applied pressure gradients in a horizontal pipe. These problems are simple enough to constitute an excellent introduction to the field of non-Newtonian fluid mechanics. Students at the National Institute of Applied Sciences in Tunis perform well despite no previous knowledge of Mathematical.

## APPENDIX

### Detailed derivation of the formulations of S.L.B.M

The formulations of SLBM in the predictor step are Eqs. (22) and (23). Performing Taylor series expansion on the equilibrium distribution functions with respect to the space/time level of  $(r, t)$  gives

$$f_{\alpha}^{eq}(r - e_{\alpha}\delta_t, t - \delta_t) = f_{\alpha}^{eq}(r, t) - \delta_t D f_{\alpha}^{eq}(r, t) + \frac{\delta_t^2}{2} D^2 f_{\alpha}^{eq}(r, t) + o(\delta_t^3) \quad (5.1)$$

Where  $D = \left[ \frac{\partial}{\partial t} + e_\alpha \cdot \nabla \right]$ . Substituting the above equation into Eqs. (22) and (23), and utilizing the relationship in Eq. (13) yield

$$p^* = \sum_\alpha f_\alpha^{eq}(r, t) - \delta_t \sum_\alpha D f_\alpha^{eq}(r, t) + \frac{\delta_t^2}{2} \sum_\alpha D^2 f_\alpha^{eq}(r, t) + o(\delta_t^3)$$

$$= p(r, t) - \delta_t \left[ \frac{\partial}{\partial t} \sum_\alpha f_\alpha^{eq}(r, t) + \nabla \cdot \sum_\alpha e_\alpha f_\alpha^{eq}(r, t) \right] - \delta_t \sum_\alpha D \frac{1}{2\tau} f_\alpha^{neq}(r, t) + o(\delta_t^2) \quad (5.2)$$

$$p^* u^* = \sum_\alpha e_\alpha f_\alpha^{eq}(r - e_\alpha \delta_t, t - \delta_t)$$

$$= \sum_\alpha e_\alpha f_\alpha^{eq}(r, t) - \delta_t \sum_\alpha e_\alpha D f_\alpha^{eq}(r, t) + \frac{\delta_t^2}{2} \sum_\alpha e_\alpha D^2 f_\alpha^{eq}(r, t) + o(\delta_t^3)$$

$$= p(r, t) u(r, t) - \delta_t \left[ \frac{\partial}{\partial t} \sum_\alpha e_\alpha f_\alpha^{eq}(r, t) + \nabla \cdot \sum_\alpha (e_\alpha)_\beta (e_\alpha)_\gamma f_\alpha^{eq}(r, t) \right]$$

$$- \delta_t \sum_\alpha e_\alpha D \frac{1}{2\tau} f_\alpha^{neq}(r, t) + o(\delta_t^2) \quad (5.3)$$

Note that the compatibility condition gives

$$\sum_\alpha f_\alpha^{neq} = \sum_\alpha e_\alpha f_\alpha^{neq} = 0 \quad (5.4)$$

And we can thus derive

$$\sum_\alpha D \frac{1}{2\tau} f_\alpha^{neq} = \sum_\alpha \frac{\partial}{\partial t} \left[ \frac{1}{2\tau} f_\alpha^{neq} \right] + \sum_\alpha e_\alpha \cdot \nabla \left[ \frac{1}{2\tau} f_\alpha^{neq} \right]$$

$$= \frac{\partial}{\partial t} \left[ \frac{1}{2\tau} \sum_\alpha f_\alpha^{neq} \right] + \nabla \cdot \left[ \frac{1}{2\tau} \sum_\alpha e_\alpha f_\alpha^{neq} \right]$$

$$= 0$$

$$\sum_\alpha e_\alpha D \frac{1}{2\tau} f_\alpha^{neq}(r, t) = \sum_\alpha \frac{\partial}{\partial t} \left[ \frac{1}{2\tau} e_\alpha f_\alpha^{neq} \right] + \sum_\alpha e_\alpha \cdot \nabla \left[ \frac{1}{2\tau} f_\alpha^{neq} \right]$$

$$= \frac{\partial}{\partial t} \left[ \frac{1}{2\tau} \sum_\alpha e_\alpha f_\alpha^{neq} \right] + \nabla \cdot \sum_\alpha (e_\alpha)_\beta (e_\alpha)_\gamma \left[ \frac{1}{2\tau} f_\alpha^{neq} \right]$$

$$= \nabla \cdot \sum_\alpha (e_\alpha)_\beta (e_\alpha)_\gamma \left[ \frac{1}{2\tau} f_\alpha^{neq} \right] \quad (5.5)$$

Therefore, Eqs. (-35) and (-36) can be reduced to

$$p^* = p(r, t) - \delta_t \left[ \frac{\partial p}{\partial t} + \nabla \cdot \sum_\alpha e_\alpha f_\alpha^{eq}(r, t) + o(\delta_t^2) \right] \quad (5.6)$$

$$p^* u^* = p(r, t) u(r, t) - \delta_t \left[ \frac{\partial p u}{\partial t} + \nabla \cdot \sum_\alpha (e_\alpha)_\beta (e_\alpha)_\gamma \left[ f_\alpha^{eq}(r, t) + \frac{1}{2\tau} f_\alpha^{neq}(r, t) \right] + o(\delta_t^2) \right] \quad (5.7)$$

Which means that Eqs. (22) And (23) recover Eqs. (18) And (19) with second order accuracy.

Similarly, the evolution equation of SLBM in the corrector step (i.e., Eq. (26)) can be expanded as

$$\frac{p^{n+1} u^{n+1} - p^n u^n}{\delta_t} = \frac{1}{\delta_t} \sum_\alpha e_\alpha \left[ \tilde{f}_\alpha^-(r + 0.5 e_\alpha \delta_t, t - 0.5 \delta_t) - \tilde{f}_\alpha^-(r - 0.5 e_\alpha \delta_t, t - 0.5 \delta_t) \right]$$

$$= \frac{1}{\delta_t} \sum_\alpha e_\alpha \left[ \nabla \cdot e_\alpha \delta_t \tilde{f}_\alpha^-(r, t - 0.5 \delta_t) + o(\delta_t^3) \right]$$

$$= \nabla \cdot \sum_\alpha (e_\alpha)_\beta (e_\alpha)_\gamma \tilde{f}_\alpha^-(r, t - 0.5 \delta_t) + o(\delta_t^2) \quad (5.8)$$

It is demonstrated that the Eq. (26) recovers the space derivative term in the macroscopic Eq. (24) with second order accuracy. And the approximated term is at the time level of  $(t - 0.5 \delta_t)$ , which reflects the central difference scheme in time marching and thus ensures second order accuracy both in time and in space".

#### NOMENCLATURE

g : gravitational acceleration (m/s<sup>2</sup>)

Q: volumetric flow rate (m<sup>3</sup>/s)

L : pipe length (m)

n : power-law exponent

$\Delta P$  : pressure difference (Pa)

R : pipe radius (m)

$R_1, R_2$  : annulus radiuses (m)

r : radial position (m)

$v_z$  : velocity (m/s)

z : axial position (m)

$\kappa$  : power-law consistency index (N.s<sup>n</sup>/m<sup>2</sup>)

$\delta$  : film thickness (m)

$\lambda$  : relaxation parameter (s)

$\eta$  : viscosity (kg/m.s<sup>2</sup>)

$\eta_0$  : Zero-shear viscosity (kg/m.s<sup>2</sup>)

$\eta_\infty$  : Infinite-shear viscosity (kg/m.s<sup>2</sup>)

$\rho$  : density (kg/m<sup>3</sup>)

$\tau_0$  : yield stress (kg/m.s)

$\tau_{rz}$  : Shear stress (kg/m.s)

#### REFERENCES

1. Reiner M, Leaderman H. Deformation, strain, and flow. *Physics Today* 1960; 13: 47
2. Maxwell JC. IV. On the dynamical theory of gases. *Philosophical transactions of the Royal Society of London* 1867: 49-88.
3. Goddard J, Miller C. An inverse for the Jaumann derivative and some applications to the rheology of viscoelastic fluids. *Rheologica Acta* 1966; 5: 177-184.
4. Bird RB, Hassager O, Abdel-Khalik S. Co-rotational rheological models and the Goddard expansion. *AIChE Journal* 1974; 20: 1041-1066.
5. Green AE, Rivlin RS. The mechanics of non-linear materials with memory. *Archive for Rational Mechanics and Analysis* 1957; 1: 1-21.
6. Rivlin R, Sawyers K, Nonlinear continuum mechanics of viscoelastic fluids, in: *Collected Papers of RS Rivlin*, Springer, 1971, pp. 2002-2031.
7. Bird RB. Useful non-Newtonian models. *Annual Review of Fluid Mechanics* 1976; 8: 13-34.
8. Aharonov E, Rothman DH. Non-Newtonian flow (through porous media): A lattice-Boltzmann method. *Geophysical Research Letters* 1993; 20: 679-682.
9. Gabbaneli S, Drazer G, Koplik J. Lattice Boltzmann method for non-Newtonian (power-law) fluids. *Physical review E* 2005; 72: 046312.
10. Giraud L, d'Humières D, Lallemand P. A lattice-Boltzmann model for visco-elasticity. *International Journal of Modern Physics C* 1997; 8: 805-815.
11. Sullivan S, Gladden L, Johns M. Simulation of power-law fluid flow through porous media using lattice Boltzmann techniques. *Journal of Non-Newtonian Fluid Mechanics* 2006; 133: 91-98.
12. Yoshino M, Hotta Y-h, Hirozane T, Endo M. A numerical method for incompressible non-Newtonian fluid flows based on the lattice Boltzmann method. *Journal of non-newtonian fluid mechanics* 2007; 147: 69-78.
13. Wang L, Mi J, Meng X, Guo Z. A localized mass-conserving lattice Boltzmann approach for non-Newtonian fluid flows.

- Communications in Computational Physics 2015; 17: 908-924.
14. Chai Z, Shi B, Guo Z, Rong F. Multiple-relaxation-time lattice Boltzmann model for generalized Newtonian fluid flows. *Journal of Non-Newtonian Fluid Mechanics* 2011; 166: 332-342.
  15. Li Q, Hong N, Shi B, Chai Z. Simulation of power-law fluid flows in two-dimensional square cavity using multi-relaxation-time lattice Boltzmann method. *Communications in Computational Physics* 2014; 15: 265-284.
  16. Nejat A, Abdollahi V, Vahidkhah K. Lattice Boltzmann simulation of non-Newtonian flows past confined cylinders. *Journal of Non-Newtonian Fluid Mechanics* 2011; 166: 689-697.
  17. Ouared R, Chopard B. Lattice Boltzmann simulations of blood flow: non-Newtonian rheology and clotting processes. *Journal of statistical physics* 2005; 121: 209-221.
  18. Boyd J, Buick JM, Green S. Analysis of the Casson and Carreau-Yasuda non-Newtonian blood models in steady and oscillatory flows using the lattice Boltzmann method. *Physics of Fluids* 2007; 19: 093103.
  19. Ashrafizaadeh M, Bakhshaei H. A comparison of non-Newtonian models for lattice Boltzmann blood flow simulations. *Computers & Mathematics with Applications* 2009; 58: 1045-1054.
  20. Svec O, Skoček J, Stang H, Geiker MR, Roussel N. Free surface flow of a suspension of rigid particles in a non-Newtonian fluid: A lattice Boltzmann approach. *Journal of Non-Newtonian Fluid Mechanics* 2012; 179: 32-42.
  21. Fallah K, Khayat M, Borghei MH, Ghaderi A, Fattahi E. Multiple-relaxation-time lattice Boltzmann simulation of non-Newtonian flows past a rotating circular cylinder. *Journal of Non-Newtonian Fluid Mechanics* 2012; 177: 1-14.
  22. Vikhansky A. Lattice-Boltzmann method for yield-stress liquids. *Journal of Non-Newtonian Fluid Mechanics* 2008; 155: 95-100.
  23. Sterling JD, Chen S. Stability analysis of lattice Boltzmann methods. *Journal of Computational Physics* 1996; 123: 196-206.
  24. Succi S. *The lattice Boltzmann equation: for fluid dynamics and beyond*. Oxford university press, 2001.
  25. Lallemand P, Luo L-S. Theory of the lattice Boltzmann method: Dispersion, dissipation, isotropy, Galilean invariance, and stability. *Physical Review E* 2000; 61: 6546.
  26. d'Humières D. Multiple-relaxation-time lattice Boltzmann models in three dimensions. *Philosophical Transactions of the Royal Society of London A: Mathematical, Physical and Engineering Sciences* 2002; 360: 437-451.
  27. Karlin I, Ferrante A, Öttinger HC. Perfect entropy functions of the lattice Boltzmann method. *EPL (Europhysics Letters)* 1999; 47: 182.
  28. Latt J, Chopard B. Lattice Boltzmann method with regularized pre-collision distribution functions. *Mathematics and Computers in Simulation* 2006; 72: 165-168.
  29. Chen Z, Shu C, Tan D, Wu C. On improvements of simplified and highly stable lattice Boltzmann method: Formulations, boundary treatment, and stability analysis. *International Journal for Numerical Methods in Fluids* 2018; 87: 161-179.
  30. Chen Z, Shu C, Wang Y, Yang LM, Tan D. A Simplified Lattice Boltzmann Method without Evolution of Distribution Function. *Advances in Applied Mathematics and Mechanics* 2017; 9: 1-22.
  31. Chen Z, Shu C, Tan D. A simplified thermal lattice Boltzmann method without evolution of distribution functions. *International Journal of Heat and Mass Transfer* 2017; 105: 741-757.
  32. Chen Z, Shu C, Tan D, Niu X, Li Q. Simplified multiphase lattice Boltzmann method for simulating multiphase flows with large density ratios and complex interfaces. *Physical Review E* 2018; 98: 063314.
  33. Chen Z, Shu C, Zhang L. A simplified axisymmetric lattice Boltzmann method for incompressible swirling and rotating flows. *Physics of Fluids* 2019; 31: 023605.
  34. Chen Z, Shu C, Tan D. Immersed boundary-simplified lattice Boltzmann method for incompressible viscous flows. *Physics of Fluids* 2018; 30: 053601.
  35. Behrend O, Harris R, Warren P. Hydrodynamic behavior of lattice Boltzmann and lattice Bhatnagar-Gross-Krook models. *Physical Review E* 1994; 50: 4586.
  36. Tian F-B, Bharti RP, Xu Y-Q. Deforming-Spatial-Domain/Stabilized Space-Time (DSD/SST) method in computation of non-Newtonian fluid flow and heat transfer with moving boundaries. *Computational Mechanics* 2014; 53: 257-271.
  37. Chen Z, Shu C, Tan DS. The Simplified Lattice Boltzmann Method on Non-Uniform Meshes. *Communications in Computational Physics* 2018; 23: 1131-1149.
  38. Wang Y, Shu C, Yang L, Yuan H. A decoupling multiple-relaxation-time lattice Boltzmann flux solver for non-Newtonian power-law fluid flows. *Journal of Non-Newtonian Fluid Mechanics* 2016; 235: 20-28.
  39. [http://library.wolfram.com/infocenter/search/?search\\_results=1;search\\_person\\_id=1536](http://library.wolfram.com/infocenter/search/?search_results=1;search_person_id=1536).
  40. Wolfram, S., *Mathematica®, A System for doing Mathematics by Computer*, Addison- Wesley, Redwood City, 1988.
  41. <http://www.polymath-software.com>
  42. Cutlip, M. B. and M. Shacham, *Problem Solving in Chemical Engineering with Numerical Methods*, Prentice Hall, Upper Saddle River, 1999.
  43. Wilkes, J. O., *Fluid Mechanics for Chemical Engineers*, Prentice Hall, Upper Saddle River, 1999.